Draft version October 20, 2023
Typeset using LaTeX twocolumn style in AASTeX631

GalactISM simulations I: resolved star formation and galactic outflows across main sequence and quenched galactic environments

Sarah M. R. Jeffreson[1]

[1] Center for Astrophysics, Harvard & Smithsonian, 60 Garden Street, Cambridge MA, USA

ABSTRACT

We present a suite of six high-resolution chemo-dynamical simulations of isolated galaxy discs, spanning observed main sequence and quenched, bulge-dominated (early type) galactic environments. We compare and contrast the physics driving star formation and stellar feedback amongst these galaxies. We find that the star formation rate in five out of six galaxies is regulated by the mid-plane gas pressure $P_{\rm tot}$, in agreement with the Pressure-Regulated Feedback-Modulated (PRFM) star formation theory. The mass-loading of galactic outflows is strongly coupled to the clustering of supernova explosions, which similarly varies strongly with Ω, leading to smoother gas discs in bulge-dominated galaxies. The equation of state of the star-forming gas therefore also varies strongly with the degree of rotational support provided by the galactic angular momentum Ω, so that the bulge-dominated galaxies have higher mid-plane densities, lower velocity dispersions, and higher molecular gas fractions than their main sequence counterparts. In one early type galaxy, we reproduce morphological quenching of the star formation efficiency (SFE) in agreement with observations, and show that it is induced in large part by non-axisymmetric torques on the scales of giant molecular clouds, driving prograde rotation of these overdensities and producing a transition away from pressure regulation.

1. INTRODUCTION

Since the first detections of cold gas in elliptical, early type galaxies (ETGs) at low redshift (Wiklind & Rydbeck 1986; Phillips et al. 1987), the presence of star-forming gas in such galaxies has been shown to be relatively common. Molecular gas has been detected in at least 22 per cent of local ETGs (Welch & Sage 2003; Combes et al. 2007; Young et al. 2011), and some of the most massive ETGs are found to have large molecular gas reservoirs between 10^9 and 10^{11} solar masses (e.g. Salomé & Combes 2003; Russell et al. 2016; O'Sullivan et al. 2018; Russell et al. 2019).

With the recent advent of high-sensitivity sub-millimeter interferometers, it has become possible to resolve these molecular gas reservoirs in great detail, and even to distinguish individual giant molecular clouds (GMCs) within them (Utomo et al. 2015; Liu et al. 2021a; Williams et al. 2023). Such studies demonstrate that the interstellar media of lenticular and elliptical galaxies display very different properties to their main sequence spiral galaxy counterparts, forming very smooth gas disks that more-closely resemble protoplanetary disks than they do galaxies (Davis et al. 2022). A large fraction of these ETGs also display a suppressed star formation efficiency (SFE), with cold gas and molecular gas depletion times that are elevated by up to an order of magnitude, relative to the highest values measured in main sequence galaxies. Interestingly, these elongated depletion times are not seen in all ETGs: the average factor reduction in SFE in these ellipticals, relative to spiral galaxies is around 2.5 times (Davis et al. 2014a).

The suppression of the SFE in bulge-dominated galaxies is also a prominant feature in large galaxy surveys that directly detect cold gas over a range of redshifts (e.g. Saintonge et al. 2012; Tacconi et al. 2018; Colombo et al. 2020). Computing molecular gas masses via the dust reddening of optical spectra in the SDSS sample, Piotrowska et al. (2022) have shown a suppression of the SFE in quenched galaxies by two orders of magnitude, comparable to the factor reduction in their gas fractions. Across the EDGE-CALIFA survey (Colombo et al. 2020), it is found that the offset from the galactic main sequence for low gas-fraction galaxies is driven predominantly by a large drop in their SFEs, relative to a much weaker correlation with the molec-

Corresponding author: Sarah M. R. Jeffreson et al.
sarah.jeffreson@cfa.harvard.edu

ular gas fraction. Such data indicate that the quenching of star formation occurs both due to an ejection of gas from galaxies, driven perhaps by AGN feedback or strong galactic outflows REF, and due to the quenching of star formation within the remaining gas. A mechanism shown to produce the latter effect in numerical simulations is 'morphological quenching' (Martig et al. 2009, 2013; Gensior et al. 2020), whereby stabilising torques due to the rapid rate of galactic rotation in bulge-dominated environments prevents the collapse of cold gas to form new stars.

To correctly predict and therefore understand the pathways to star formation quenching throughout the course of galaxy evolution, it is therefore necessary to correctly model variations in the physics driving star formation and stellar feedback in the interstellar media of both star-forming and quenched galaxies. Unfortunately, state-of-the-art hydrodynamical cosmological simulations are currently unable to model these variations. Of the Illustris (Vogelsberger et al. 2014), Illustris-TNG (Nelson et al. 2018) and EAGLE (Schaye et al. 2015) simulations, Illustris-TNG displays the best qualitative agreement with trends in the SDSS survey, but substantially over-estimates the stellar mass at which quenching sets in, associated with substantial quantitative differences in the SFEs and gas fractions of high-mass galaxies (Piotrowska et al. 2022).

This is perhaps unsurprising, considering the simplifications made in the modelling of star formation, stellar feedback and galactic winds in such cosmological simulations. These simulations lack the resolution to model the star-forming ISM, and so adopt subgrid treatments that are typically calibrated to observed scalings in low-redshift, main sequence galaxies (in the case of star formation and stellar feedback) or that are tuned to reproduce key galaxy scaling relations (in the case of wind mass and energy loading, see Smith et al. 2023 and citations therein). In particular, the SFE is commonly set according to the relationship between star formation rate and gas density in nearby spiral galaxies (e.g. Springel & Hernquist 2003): the same relationship that is shifted systematically for the interstellar media of ETGs.

As such, one of the key goals of the Learning the Universe Simons Collaboration (and one of its predecessors, the SMAUG collaboration) is to substitute the existing, empirically-calibrated or tuned subgrid prescriptions in cosmological simulations with models that are calibrated based on higher resolution simulations, which capture the relevant physics on smaller scales. The connection between the high-resolution ISM simulations and the lower-resolution cosmological simulations will be facilitated by physically-motivated analytic models such as the "Pressure-Regulated Feedback-Modulated" (PRFM) star formation theory (Ostriker et al. 2010; Ostriker & Kim 2022; Hassan et al. 2023). The collaboration therefore aims to produce cosmological simulations that no longer require empirical calibration or tuning, allowing for the predictive modelling of star formation quenching, among other physics.

In this paper, we introduce the first six of the "GalactISM" simulations: a suite of high-resolution, chemodynamical isolated galaxy simulations spanning observed, dynamically-diverse star-forming environments. Here we consider environments spanning from the galactic main sequence of spiral galaxies to the population of low gas-fraction, fast-rotating, quenched ETGs at low redshift. The aim of these simulations is to explicitly model environmental trends in the SFR, SFE and gas density-pressure variation across these galactic environments, and so to identify (1) where physically-motivated analytic theory (such as PRFM) can be used to model these relationships, and (2) where complex or non-linear variations arise, that might be accounted for via statistical or learned modelling of the scatter about the analytic theory—another facet of the Learning the Universe collaboration.

The GalactISM simulations are complementary to the "TIGRESS" and "TIGRESS-NCR" frameworks—magneto-hydrodynamic (MHD) simulations that provide a higher spatial resolution in the non-molecular gas phases,[1] allowing for full UV radiative transfer via adaptive ray-tracing. By contrast, the GalactISM simulations use the mechanical HII region feedback prescription introduced in Jeffreson et al. (2021), appropriate to marginally-resolved HII regions. At the slightly lower resolution of GalactISM we can model entire galaxies and their star-forming gas reservoirs relatively efficiently, allowing for the potential influence of inward radial mass transport (e.g. Krumholz & Burkert 2010; Goldbaum et al. 2015; Krumholz et al. 2018), and for the later inclusion of a circumgalactic medium, necessary for the modelling of high gas-fraction, high-redshift galactic environments. We also produce a statistical sample of around $60,000$ GMCs across these six simulations.

[1] The TIGRESS simulations are run with the grid-based Athena code (Stone et al. 2008; Stone & Gardiner 2009), achieving a spatial resolution of 2 pc throughout the gas reservoir. The GalactISM simulations are run with the adaptive-mesh code Arepo, with a mass resolution of 859 $M_{\odot}$, corresponding to a spatial resolution of ~ 1 pc in the dense, molecular gas, but increasing up to ~ 30 pc in the hottest, ionised gas.

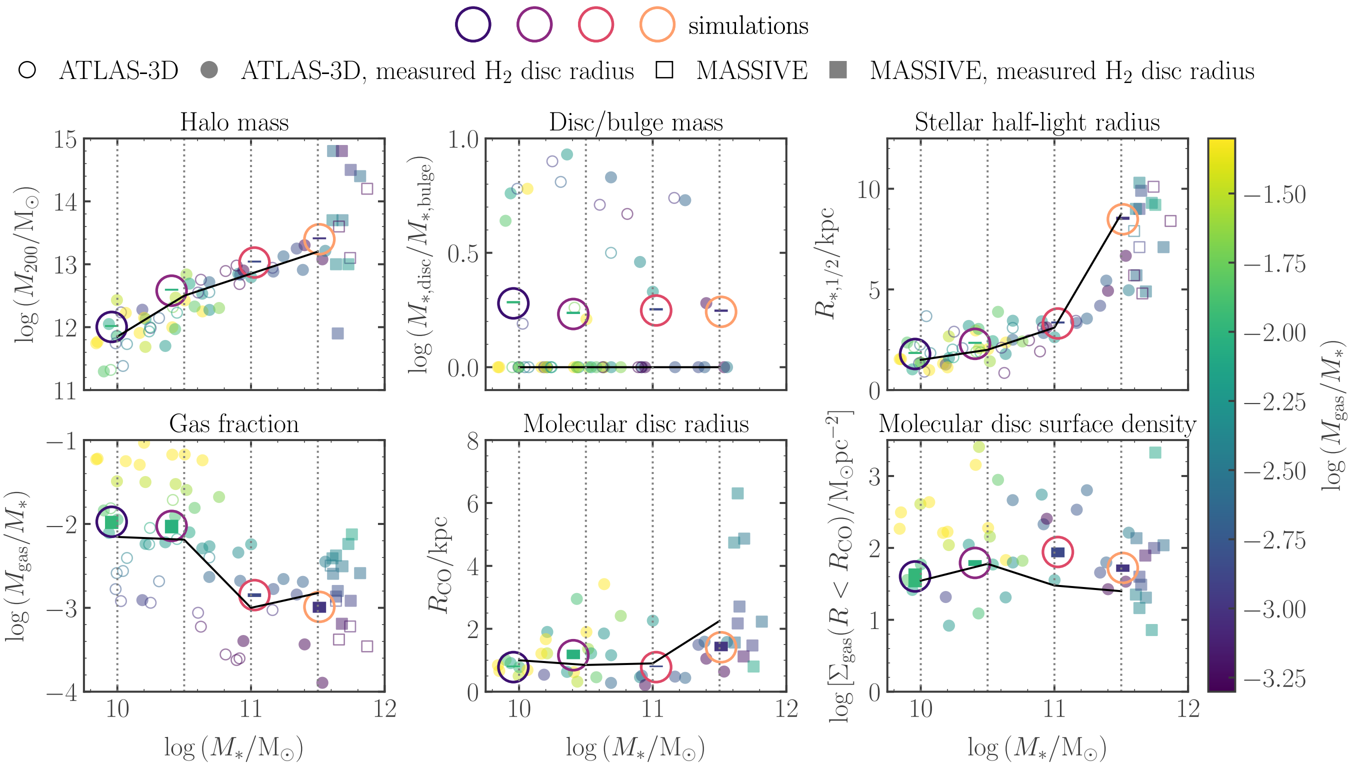

Figure 1. Physical properties of the simulated early type galaxies, compared to observed galaxies from the ATLAS-3D (circular transparent data points) and MASSIVE (square transparent data points) galaxy surveys. Unfilled data points represent observed galaxies with no measured values of the molecular gas disc size R_{CO} (centre bottom panel), and so no measured values of the molecular gas surface density $\Sigma_{\mathrm{H_2,CO}}$ (right-hand bottom panel) exceeds a value of 10 $\mathrm{M_\odot pc^{-2}}$. Black lines represent the median observed values of each physical quantity in stellar mass bins centred on $M_* = 10^{10}$, $10^{10.5}$, 10^{11} and $10^{11.5}$ $\mathrm{M_\odot}$. The circled vertical bars represent the values spanned by the simulated galaxies between the simulation times of 100 and 400 Myr, coloured according to their gas fractions. Our simulations roughly reproduce these median values (see Section 2.1).

Similar to the TIGRESS simulations,[2] the GalactISM simulations include stochastic modelling of the initial stellar mass function (da Silva et al. 2012, 2014; Krumholz et al. 2015), supernova feedback (Keller & Kruijssen 2020; Jeffreson et al. 2021), non-equilibrium cooling via a chemical network modelling hydrogen, carbon and oxygen (Glover & Mac Low 2007a,b; Glover et al. 2010), dust- and self-shielding of molecular hydrogen from dissociation by the interstellar radiation field (Clark et al. 2012), and an instability-based star formation criterion (Padoan et al. 2014; Gensior et al. 2020).

The remainder of the paper is structured as follows. In Section 2 we introduce the GalactISM suite, along with the numerical models used for star formation, stellar feedback, chemistry and cooling. In Section 3 we given an overview of the dynamical properties, gas phase distribution and morphology, and star-forming behaviour of our galaxies, in comparison to observed ETGs from the ATLAS-3D survey (Davis et al. 2013). Section 4 provides a systematic analysis of the properties of stellar feedback-driven galactic outflows in our simulation and their dependence on the level of supernova clustering and gravitational stability in the simulated gas disks. The scaling of the star formation rate surface density with the gas surface density, the mid-plane pressure and the ISM weight are investigated in Section 5, along with the equation of state between the gas density and pressure. We provide a detailed analysis of our morphologically-quenched galaxy simulation in Section 6, and finally conclude with a discussion and summary of our results in Section 7.

[2] We note that all implemented numerical models are different to those incorporated into the TIGRESS framework, but model the same physical processes. See Kim et al. (2020, 2023b,a) for full details of the TIGRESS and TIGRESS-NCR models.

2. SIMULATION SUITE

The six chemo-dynamical isolated galaxy simulations presented in this work consist of one large spiral (Milky Way-like) galaxy, one dwarf spiral (NGC 300-like) galaxy, and four early type (ETG) galaxies. The physical properties of the ETG simulations are matched to the

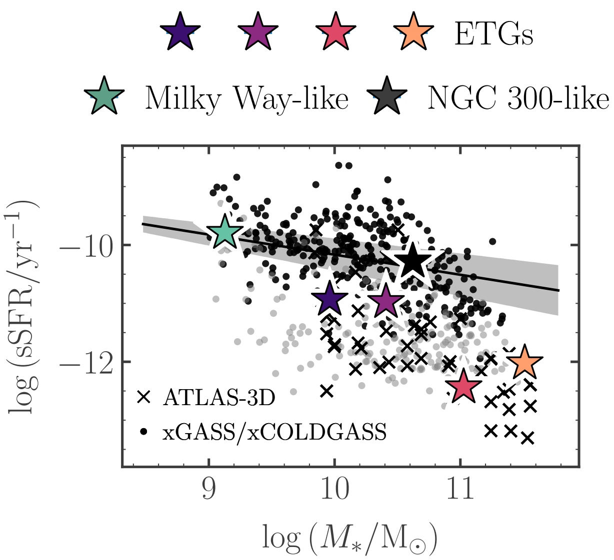

Figure 2. Each of the six isolated galaxy simulations (stars) in the plane of total stellar mass M_* vs. specific star formation rate sSFR. Black data points represent atomic and molecular gas detections, respectively, from the xGASS (Catinella et al. 2018) and xCOLDGASS (Saintonge et al. 2017) surveys, while grey data points represent non-detections. Black crosses represent data from the ATLAS-3D survey (Davis et al. 2013). The galactic main sequence as defined in the former work in is given by the black solid line and shaded region.

observations of elliptical galaxies from the ATLAS-3D and MASSIVE surveys. Together, the simulated galaxies span over two orders of magnitude in total stellar mass and specific star formation rate (see Figure 2), from the galactic main sequence (black line) down to the quenched galaxy population below.

2.1. *Initial conditions*

We generate initial conditions for our simulations using the MakeNewDisk model (Springel et al. 2005). The input parameters for the ETG simulations are shown in Table 2. We use the Agora initial condition for the Milky Way-like simulation (Kim et al. 2014, see Section 2.1.2). The dark matter halo is of Navarro et al. (1997) (NFW) type, and the stellar and gas discs follow an exponential form. The stellar bulge follows a Plummer (1911) profile in the ETG initial conditions and a Hernquist (1990) profile in the Milky Way-like initial condition. Our median gas cell mass is 859 $\mathrm{M}_\odot$.

2.1.1. *Early type galaxies*

Our initial conditions for the ETG galaxies have stellar masses of $M_* = 10^{10}, 10^{10.5}, 10^{11}$ and $10^{11.5}$ $\mathrm{M}_\odot$, covering the range of masses spanned by the observed elliptical galaxies from the ATLAS-3D and MASSIVE surveys (Cappellari et al. 2013; Davis et al. 2019). We choose the virial halo masses M_{200} and stellar half-light radii $R_{*,1/2}$ according to the median observed values in each of these four stellar mass bins (Cappellari et al. 2011; Davis et al. 2014a, 2019), given as black lines in Figure 1. The corresponding properties of the simulated galaxies are given by the circled bars: the vertical span of each bar shows the variation in each galaxy property over the set of simulation times for which we analyse the data, from 100 to 400 Myr after initialisation. We set the gas-to-stellar fraction $M_{\rm gas}/M_*$ (lower left panel of Figure 1) according to the same set of observations. Due to the observed drop in the gas fraction between stellar masses of $M_* = 10^{10.5}$ and 10^{11} $\mathrm{M}_\odot$, our two lowest-mass galaxies are assigned gas fractions of approximately one per cent, while the two highest-mass galaxies are assigned gas fractions of ~ 0.1 per cent.

We set the disc-to-bulge mass ratio of our simulated galaxies to $M_{*,\rm disc}/M_{*,\rm bulge} = 0.2$, in contrast to the median observed value of $M_{*,\rm disc}/M_{*,\rm bulge} \sim 0$ (pure ellipticals). This will allow us, in a future paper, to directly compare to the detailed molecular cloud properties in the ETG simulations to observations of the resolved molecular cloud populations in the lenticular galaxy NGC 4429, studied by Liu et al. (2021b).

Finally, we set the scale radii of our gas discs according to measurements of the mean CO-luminous molecular gas surface densities $\Sigma_{\rm H_2,CO}(R < R_{\rm CO})$ inside the radii $R_{\rm CO}$ at which this surface density drops to a value of 10 $\mathrm{M}_\odot\mathrm{pc}^{-2}$ (Davis et al. 2013, 2019, Davis et al. in preparation). The observed and simulated values of $R_{\rm CO}$ and $\Sigma_{\rm H_2,CO}(R < R_{\rm CO})$ are shown in the bottom centre and bottom right-hand panels of Figure 1, respectively. The CO-luminous gas fraction is computed for each simulation output using the DESPOTIC astrochemistry and radiative transfer model (Krumholz 2013, 2014), as described in Appendix A.

2.1.2. *Milky Way-like galaxy*

For our Milky Way-like simulation, we use the isolated disc initial condition generated for the Agora comparison project (Kim et al. 2014). This initial condition is designed to resemble a Milky Way-like galaxy at redshift $z \sim 0$. It has a dark matter halo mass of $M_{200} = 1.07\times10^{12} M_\odot$, a virial radius of $R_{200} = 205$ kpc, a halo concentration of $c = 10$ and a spin parameter of $\lambda = 0.04$. The stellar bulge has a mass of $3.437\times10^9\mathrm{M}_\odot$, while the exponential disc has a mass of $4.297\times10^{10}\mathrm{M}_\odot$, a scale-length of 3.43 kpc, and a scale-height of 0.34 kpc. The bulge to stellar disc ratio is 0.125 and the overall gas fraction is 0.18.

2.1.3. *NGC 300-like galaxy*

Table 1. Input parameters for MakeNewDisk, used to create initial conditions for the early type galaxy simulations. These include the halo concentration parameter c, velocity V_{200} at the virial radius, spin parameter λ, stellar disc mass $M_{*,\mathrm{d}}$, bulge mass M_b, gas fraction relative to the stellar disc $M_\mathrm{gas}/M_{*,\mathrm{d}}$, ratio of the stellar disc scale-height to scale-radius $h_{*,\mathrm{d}}/R_{*,\mathrm{d}}$, ratio of the gas to the stellar scale radius $R_\mathrm{gas}/R_{*,\mathrm{d}}$, and mass resolutions of the halo (ϵ_halo), stellar particles (ϵ_*) and gas cells (ϵ_gas).

Stellar mass/M$_\odot$	**10^{10}**	**$10^{10.5}$**	**10^{11}**	**$10^{11.5}$**
c	8.6	7.4	6.7	6.4
V_{200}/km s^{-1}	130	200	280	370
λ	0.04	0.04	0.04	0.04
$M_{*,\mathrm{d}}/\mathrm{M}_\odot$	2×10^9	6.3×10^9	2×10^{10}	6.3×10^{10}
$M_\mathrm{b}/\mathrm{M}_\odot$	8×10^9	2.5×10^{10}	8×10^{10}	2.5×10^{11}
$M_\mathrm{gas}/M_{*,\mathrm{d}}$	0.07	0.07	0.007	0.007
$h_{*,\mathrm{d}}/R_{*,\mathrm{d}}$	0.1	0.1	0.1	0.1
$R_\mathrm{gas}/R_{*,\mathrm{d}}$	0.07	0.06	0.04	0.04
$R_\mathrm{b}/R_{*,\mathrm{d}}$	1.35	1.85	2.8	8.75
$\epsilon_\mathrm{halo}/\mathrm{M}_\odot$	1.25×10^5	1.25×10^5	1.25×10^5	1.25×10^5
$\epsilon_*/\mathrm{M}_\odot$	5×10^3	5×10^3	5×10^3	5×10^3
$\epsilon_\mathrm{gas}/\mathrm{M}_\odot$	1×10^3	1×10^3	1×10^3	1×10^3

We use the NGC 300-like initial condition presented in Jeffreson et al. (2023), which has no stellar buge, a dark matter halo of mass $M_{200} = 8.3 \times 10^{10} M_\odot$, a stellar disc of mass $1 \times 10^9 M_\odot$, and a gas disc of mass $2 \times 10^9 \mathrm{M}_\odot$ (giving a gas fraction of 68 per cent), all with identical mass resolution to the Milky Way-like galaxy. The dark matter halo has a concentration parameter of $c = 15.4$, a spin parameter of $\lambda = 0.04$, and a circular velocity of $V_{200} = 76$ km s^{-1} at the virial radius. The stellar and gas discs are of exponential form: the stellar disc has a scale-length of 1.39 kpc, while the gas disc has a scale-length of 3.44 kpc. Both the stellar and gas discs have an initial scale-height of 0.28 kpc.

2.1.4. *Galactic rotation curves*

In Figure 3 we show the mid-plane circular velocity of each simulated galaxy as a function of galactocentric radius R (thick transparent lines). We also show the separate components of the circular velocity $v_\mathrm{circ}^2 = R\mathrm{d}\Phi/\mathrm{d}R$ that are contributed by the gravitational potential Φ_gas due to the gas particles in the simulation, Φ_DM due to the dark matter particles, $\Phi_{*,\mathrm{disc}}$ due to the stellar disc, and $\Phi_{*,\mathrm{bulge}}$ due to the stellar bulge. The circular velocity of the NGC 300-like galaxy is around 25 per cent higher than the value observed by Westmeier et al. (2011), which varies from 50 to 80 km/s between galactocentric radii of 0.3 and 6 kpc, while ours has an average value of 100 km/s. Our simulated value is more typical of other dwarf spiral galaxies, such as M33 (e.g. Koch et al. 2018).

We note that the rate of galactic rotation is highest (~ 300 km/s) in the ETG of stellar mass $M_* = 10^{11}$ M$_\odot$, owing to the higher concentration of its stellar bulge. While this galaxy does not have the highest stellar mass, this mass is concentrated within the smallest stellar half-light radius. By contrast, the Milky Way-like and NGC300-like galaxies (right-hand panels) have rotation curves that are dominated by their dark matter and stellar/gas disc components, with the stellar bulge component making only a negligible or zero contribution to the circular velocity. The elevated bulge-induced rate of rotation in the $M_* = 10^{11}$ M$_\odot$ ETG is an important feature of this simulation, to which we will later return.

2.2. *Hydrodynamics, chemistry, star formation and feedback*

The initial conditions described in Section 2.1 are evolved using the moving-mesh hydrodynamics code AREPO (Springel 2010). In particular, the gas reservoir is modelled using an unstructured moving mesh that is defined by the Voronoi tesselation about a discrete set of points, moving with the local gas velocity. A hybrid TreePM gravity solver is used to calculate the gravitational acceleration vectors of the Voronoi gas cells, stellar particles and dark matter particles. We employ the native adaptive gravitational softening scheme for the gas cells, with a minimum softening length of 3 pc and a gradation of 1.5 times the Voronoi gas cell diameter. We set the softening length of the star particles to a constant value of 3 pc, and set the softening length of the dark matter particles to 280 pc, according to the convergence tests presented in Power et al. (2003).

Our models for the temperature and chemical composition of the gas in our simulations, along with the rate of star formation in this gas, and the rate of energy and momentum injection due to stellar feedback, are iden-

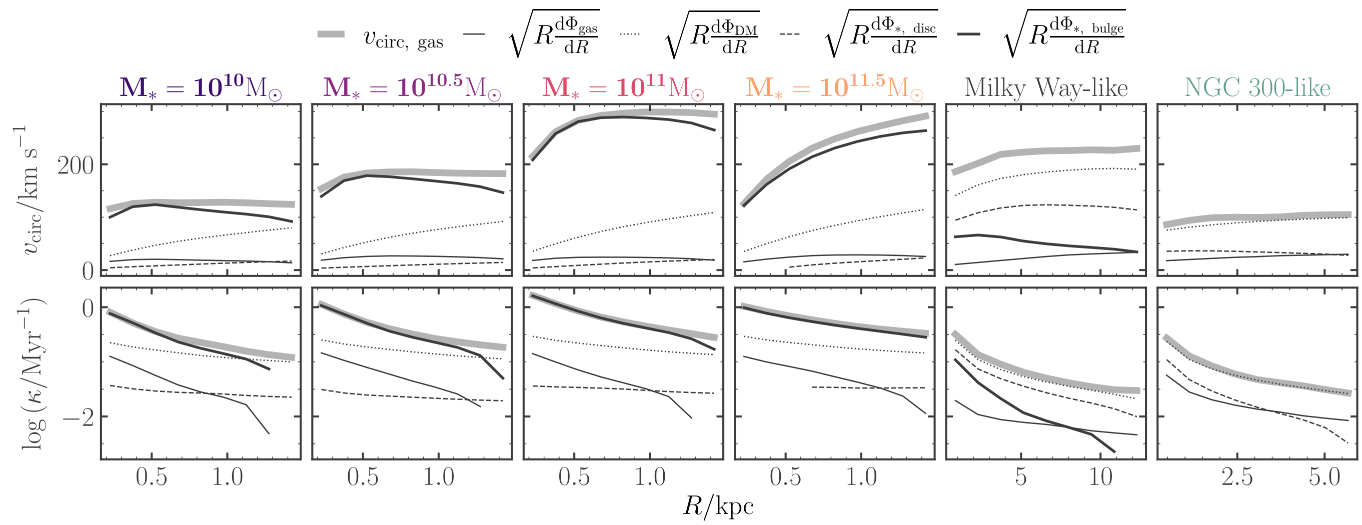

Figure 3. Mid-plane circular velocity $v_{\rm circ}$ (thick transparent lines) as a function of galactocentric radius R for each of the simulated galaxies, computed directly from the gravitational potential exerted by the gas (thin lines), dark matter (dotted lines), disc stars (dashed lines) and bulge stars (bold lines). Galactic rotation in the early type galaxies is dominated by the stellar bulge component. All early type galaxies are shown at a simulation time of 400 Myr, while the Milky Way-like galaxy is shown at a simulation time of 600 Myr.

tical to those described in Jeffreson et al. (2023). We give a brief overview of these models below, but refer the reader to the cited works for further details.

We use the non-equilibrium network for hydrogen, carbon and oxygen chemistry described in Nelson & Langer (1997) and in Glover & Mac Low (2007a,b), coupled to the atomic and molecular cooling function of Glover et al. (2010). We assume the solar value fo the dust-to-gas ratio, and use the TreeCol algorithm presented in Clark et al. (2012) to model the dust- and self-shielding of molecular hydrogen from dissociation by the interstellar radiation field, allowing us to track the non-equilibrium abundance of molecular hydrogen during the run-time of the simulation.

The star formation rate volume density in our simulation is given by

$$\frac{d\rho_{*,i}}{dt} = \begin{cases} \dfrac{\epsilon_{\rm ff}\rho_i}{t_{{\rm ff},i}},\ \rho_i \geq \rho_{\rm thresh}, T_i \leq T_{\rm thresh} & (1) \\ 0,\ \rho_i < \rho_{\rm thresh}, T_i > T_{\rm thresh} & (2) \end{cases}$$

where $t_{{\rm ff},i} = \sqrt{3\pi/(32G\rho_i)}$ is the local free-fall time-scale for the gas cell i with a mass volume density of ρ_i, and $\epsilon_{\rm ff}$ follows the parametrisation of Padoan et al. (2017), such that

$$\epsilon_{\rm ff} = 0.4\exp\left(-1.6\alpha_{\rm vir}^{0.5}\right). \quad (3)$$

The virial parameter $\alpha_{\rm vir}$ on cloud scales is computed during simulation run-time within overdense regions surrounding each star-forming gas cell, determined via a variation of the Sobolev (1960) approximation used in Gensior et al. (2020). We set an upper limit of $T_{\rm thresh} = 100$K on the temperature below which star formation is allowed to occur, and a lower limit of $\rho_{\rm thresh}/m_{\rm H}\mu = 100\ {\rm cm}^{-3}$ on the density, where μ is the mean mass per H atom, corresponding to the density of Jeans-unstable gas at our mass resolution (859 $M_\odot$) and at our minimum molecular gas temperature (~ 30K).

The star particles formed via Equations (1) and (3) generate energy and momentum from supernova explosions and pre-supernova HII regions, via the stellar feedback prescription described in Jeffreson et al. (2021). To compute the number of supernovae, ejected mass and photoionising luminosity of each star particle, we assign a stellar population drawn stochastically from a Chabrier (2003) initial stellar mass function (IMF), using the Stochastically Lighting Up Galaxies (SLUG) stellar population synthesis model (da Silva et al. 2014; Krumholz et al. 2015). An energy of 10^{51} erg per supernova is assumed, and the terminal momentum from these supernovae is explicitly calculated using the unclustered parametrisation derived from the high-resolution simulations of Gentry et al. (2017). This kinetic energy, along with the remaining thermal energy, is and injected into all gas cells surrounding each star particle. The photo-ionising luminosity associated with HII regions is converted to a momentum per unit time via the model of Jeffreson et al. (2021), following the analytic work of Matzner (2002) and Krumholz & Matzner (2009) to account for both radiation pressure and the momentum injected via the 'rocket effect': the ejection of warm ionised gas from cold molecular clouds. The gas cells inside the Strömgren radii of the HII regions are fully ionised and heated to a temperature of 7000 K.

3. STAR FORMATION AND INTERSTELLAR MEDIUM MORPHOLOGY

Quiescent, bulge-dominated galaxies have been found to have star formation efficiencies that are, on average, suppressed relative to the main sequence galaxy population (e.g. Saintonge et al. 2012; Davis et al. 2014b; Colombo et al. 2020) and to have smoother, less-fragmented interstellar media (Davis et al. 2022). Figures 5-**??** examine the star-forming and gas-morphological properties of our simulated galaxies.

3.1. *Star formation*

Figure 4 shows the star formation rate surface density Σ_* of our six simulated galaxies as a function of their cold gas surface densities $\Sigma_{\rm HI+H_2}$, their molecular gas surface densities $\Sigma_{\rm H_2}$, and their stellar surface densities Σ_*. Large circles represent averages over simulation time across the extent of each gas disc, excluding the central 300 pc.[3] Error-bars represent the corresponding interquartile ranges, where the interquartile ranges for the ETGs are too small to be displayed.

The star formation rate surface densities in Figure 4 are calculated as averages over the preceding 5 Myr, similar to the time interval traced in observations via Hα emission. Observed values from the ATLAS-3D survey are shown for comparison with the ETG simulations (transparent circles), and the observed position of NGC 300 in each plane is shown for comparison with the NGC 300-like simulation (from Kruijssen et al. 2019, black transparent star). The close agreement between simulations and observations in this Figure and in Figure 2 is an important validity check for our numerical models for star formation and stellar feedback, outlined in Section 2.

Five out of six galaxies fall along the typical power-law of index 1.5 (black solid line, left-hand panel) relating the star formation rate surface density to the cold gas surface density for main sequence galaxies (Kennicutt 1998; Bigiel et al. 2008), and have molecular gas depletion times of 1 Gyr (dashed line, second-to-left panel). However, one of the ETGs is manifestly quenched, falling substantially to the right of the power-law, with a molecular gas depletion time of around 8 Gyr. In other words, its cold gas star formation efficiency is suppressed by around 5 times, and its molecular gas star formation efficiency by nearly an order of magnitude, relative to all other galaxies. **We therefore find that the ETG simulation of stellar mass $M_* = 10^{11}$ M$_\odot$, with the most concentrated stellar bulge, is morphologically quenched.** We analyse this galaxy in detail in Section 6.

[3] We exclude the central 300 pc of each simulation from our analysis because our mass resolution is likely insufficient to accurately model the stellar feedback close to the galactic nucleus.

3.2. *Disc morphology and fragmentation*

The central and lower rows of panels in Figure 5 compare the total gas disc surface density $\Sigma_{\rm gas}$ and the molecular gas disc surface density $\Sigma_{\rm H_2}$ of all six galaxy simulations, within 2 kpc patches at face-on and edge-on viewing angles. For the ETG simulations (left four columns), these patches cover the extent of the entire gas disc. For the Milky Way-like and NGC 300-like galaxies (right two columns), with respective gas disc diameters of 30 and 12 kpc, the patch shows only a small portion of each gas disc. The top row of panels shows the edge-on stellar surface density Σ_* for each galaxy, highlighting the fact that the stellar distribution for the ETGs is bulge-dominated ($M_{\rm disc}/M_{\rm bulge} \sim 0.2$), whereas the stellar distribution is disc-dominated for the Milky Way-like galaxy ($M_{\rm disc}/M_{\rm bulge} \sim 0.9$) and for the NGC 300-like galaxy ($M_{\rm bulge} \sim 0$).

All four ETG simulations have a much smoother gas distributions than do the main sequence galaxy simulations. The quenched ETG ($M_* = 10^{11}{\rm M}_\odot$) is particularly smooth, as expected according to its low star formation rate and thus infrequent stellar feedback. The three other ETGs are manifestly fragmented into dense gas clouds, but are also much smoother than their main sequence counterparts, with much smaller feedback-driven voids of diameter < 100 pc, in contrast to the giant voids of several kpc seen in the Milky Way-like and NGC 300-like galaxies.

This lower degree of gas disc fragmentation in the early type galaxy simulations, relative to the large spiral (Milky Way-like) simulation, is in qualitative agreement with the observed sample of early type and spiral galaxies in Davis et al. (2022). In this work, the disc clumpiness of a sample of 86 spiral galaxies, as quantified by the Gini statistic, is more than double that of a sample of 15 early type, bulge-dominated galaxies, which vary from very smooth (resembling our quenched ETG simulation) to manifestly fragmented (resembling our other ETG simulations). We will discuss the physical drivers of this disc smoothness in Section 4.

Finally, we note that the gas and stellar discs of our ETG simulations develop a slight kinematic misalignment during their 400 Myr of evolution. This misalignment likely arises due to the gravitational interaction between the gas disc and the stellar bulge. The maximum

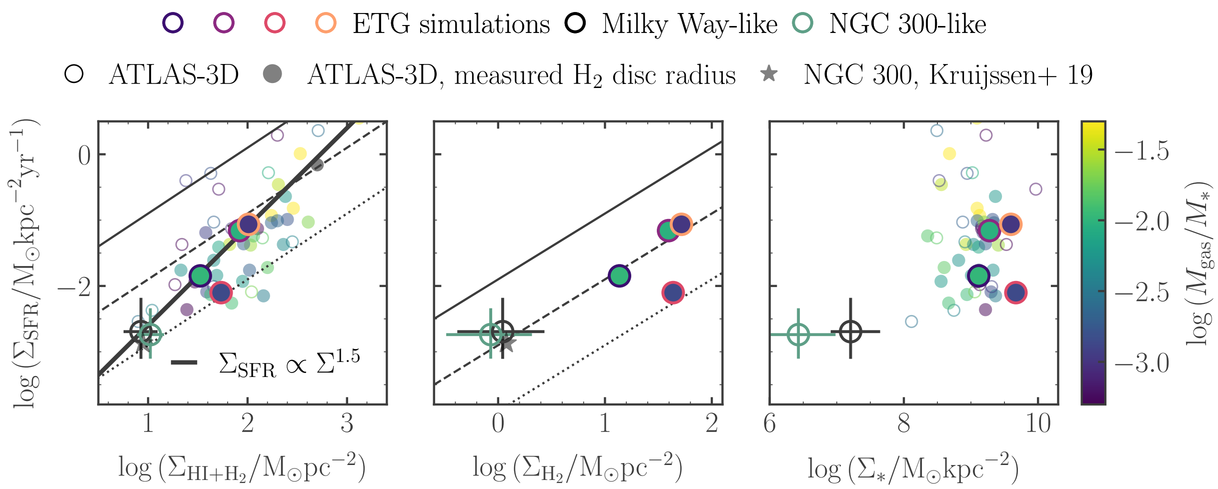

Figure 4. *Left:* Median star formation rate surface density $\Sigma_{\rm SFR}$ as a function of the cold gas (atomic plus molecular surface density) $\Sigma_{\rm HI+H_2}$, integrated across each simulated galaxy (filled circles), and measured for the galaxies in the ATLAS-3D galaxy sample Davis et al. (2013, 2014b) (transparent and unfilled circles). The colours of the data points correspond to their gas fractions, and gas depletion times of 10^8, 10^9 and 10^{10} years are given by the black solid, dashed and dotted lines, respectively. Interquartile ranges over time and galactocentric radius are given by error-bars. For the early type galaxy simulations, these are too small to be shown. *Centre:* Similar to *left* but for the molecular gas surface density $\Sigma_{\rm H_2}$. *Right:* Similar to *left* but for the median stellar surface density across the gas disc Σ_*.

skew of 3 degrees occurs for the smoothest disc with the most compact bulge ($M_* = 10^{11}{\rm M_\odot}$). Throughout this work, the term 'mid-plane' therefore refers specifically to the mid-plane of the gas disc.

3.3. *Gas phases*

The phase structure of the gas in five of our simulations is presented in Figure 6. We omit the NGC 300-like galaxy for visual clarity, but note that its gas has a very similar phase structure to that of the Milky Way-like galaxy. The two right-hand panels compare the mass-weighted distributions of gas as a function of volume density $n_{\rm H}$ and temperature T (the phase diagrams) for the Milky Way-like and quenched ETG simulations. The gas cells are clustered around the state of thermal equilibrium balancing the cooling rate (dominated in our simulations by line emission from C^+, O and Si^+) and the heating rate due to photoelectric emission from PAHs and dust grains. The region of the histogram at $T \sim 7000$ K and high volume density corresponds to the gas that is heated by the thermal feedback from HII regions, and the gas above a temperature of $\sim 20,000$ K is heated by supernova feedback.

The blue bars in the left-hand panel of Figure 6 show the partitioning of the interstellar medium into the four phases that are delineated by dashed lines in the phase diagrams: feedback-heated (SN and HII), the warm neutral medium (WNM), the cold neutral medium (CNM) and the molecular hydrogen fraction (H_2). This partitioning is chosen by eye, with the exception of the H_2 mass, which is calculated during simulation runtime using the chemical network described in Section 2. Any H_2 mass contained in the other partitions is subtracted to produce the bar plot.

We see that the cold, predominantly star-forming gas reaches much higher densities in the main sequence galaxy than in the ETGs (lower right corner of the phase diagrams). The main sequence simulation also contains a much higher fraction of warm and hot gas (pale blue bars, left-hand side), commensurate with its much larger feedback-driven bubbles and voids, as shown in Figure 5. Conversely, the ETG simulations contain a much higher fraction of cold and molecular gas (dark blue bars, left-hand side): up to 70 per cent in the quenched ETG, and 40 per cent in the other ETGs, relative to < 10 per cent of the gas in the main sequence galaxy. All of these features point to a larger degree of supernova clustering in the main sequence simulations: a point to which we will return in Section 4.

The pink bars in the left-hand panel of Figure 6 show the partitioning of the star-forming gas (molecular gas with $n_{\rm H} > 100$ cm^{-3}) into four logarithmic bins of instantaneous star formation efficiency, computed during the run-time of the simulation according to Equation (3), with darker colours corresponding to higher star formation efficiencies. While the fraction of molecular gas forming stars at low efficiency is roughly similar across the five galaxy simulations, the fraction of highly star-forming molecular gas (star formation efficiency ¿ 1 per cent) in the quenched ETG is around half that of

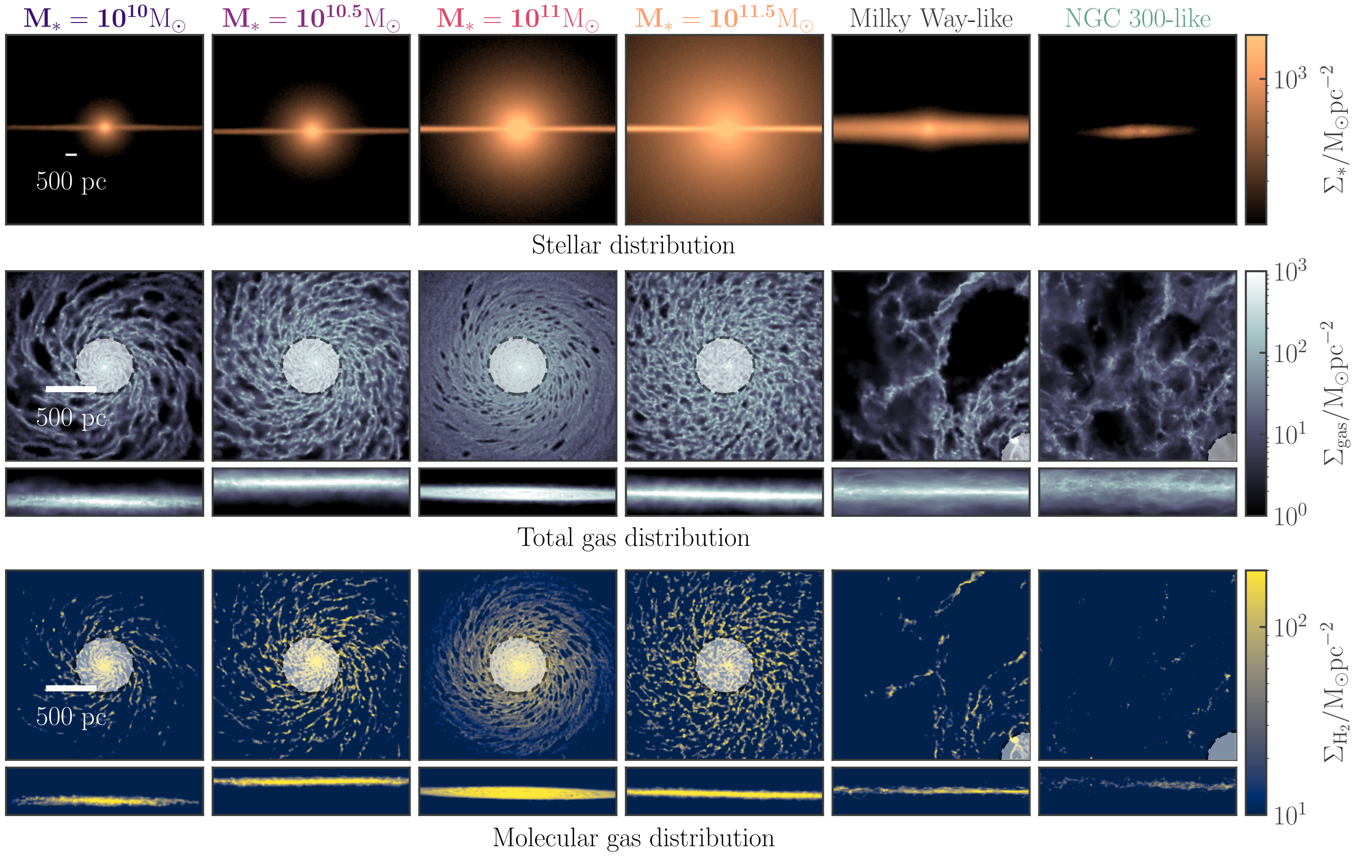

Figure 5. Surface density maps of the stellar distribution viewed parallel to the galactic mid-plane (Σ_*, upper panels), the total gas distribution viewed perpendicular to and parallel to the galactic mid-plane ($\sigma_{\rm gas}$, centre panels) and the molecular gas distribution viewed perpendicular to and parallel to the galactic mid-plane ($\Sigma_{\rm H_2}$, lower panels) for each of the simulated galaxies. All early type galaxies are shown at a simulation time of 400 Myr, while the Milky Way-like galaxy is shown at a simulation time of 600 Myr.

the other four galaxies, and it contains no molecular gas with a star formation efficiency above 10 per cent. The other three ETGs have similar molecular gas star formation efficiencies to the Milky Way-like galaxy, commensurate with the molecular Kennicutt-Schmidt relation presented in Figure 4. **The quenching of the star formation efficiency in one of our ETG simulations therefore occurs in the densest and most highly star-forming molecular gas.**

4. SUPERNOVA CLUSTERING, GALACTIC OUTFLOWS AND THE EQUATION OF STATE

Recent numerical work has shown that the spatial clustering of supernova explosions strongly affects the momentum injected into the surrounding gas (e.g. Gentry et al. 2017), and thus the strength and mass-loading of galactic outflows (Fielding et al. 2018; Smith et al. 2020). In turn, the majority of supernova clustering occurs in the most massive giant molecular clouds (Jeffreson et al. 2023), which host the majority of galactic star formation (Murray & Rahman 2010). These clouds are able to grow to large masses due to a high rate of accretion from the galactic environment, and display substantially higher lifetime star formation efficiencies than their low-mass counterparts, as they are slightly more difficult to destroy (e.g. Murray et al. 2010; Grudić et al. 2018; Jeffreson et al. 2023). In the following sections, we discuss the connection between disk gravitational stability, supernova clustering and galactic outflow strength across our main sequence and quenched galaxy simulations. We demonstrate the impact of this physics on the equation of state (pressure vs. density relation).

4.1. *Disk stability*

The top row of panels in Figure 7 demonstrates that the ETGs in our galaxy sample have a much greater level of disk stability than do the main sequence galaxies. We calculate the Toomre Q parameter for the combined cold and warm gas reservoirs ($T < 10^4$ K) via the prescriptions of Romeo & Wiegert (2011) and Romeo & Falstad (2013), which are in close agreement. Romeo & Wiegert (2011) consider the stabilising effect of disk

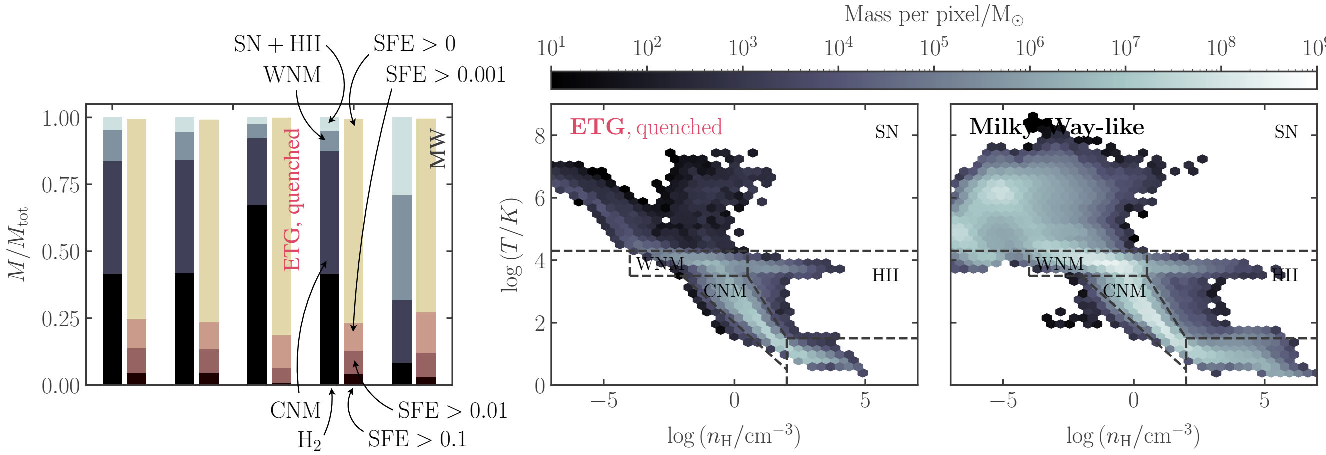

Figure 6. *Left-hand panel:* Partitioning of the gas mass in each simulation into four interstellar medium phases (blue), from warmest to coolest, as a fraction of the total gas mass in the simulation: hot gas that has received thermal energy from stellar feedback ($M_{\rm SN+HII}$), the warm neutral medium ($M_{\rm WNM}$), the cold neutral medium ($M_{\rm CNM}$), and the total molecular hydrogen reservoir ($M_{\rm H_2}$). Partitioning of the star-forming gas in each simulation into four logarithmic bins of star formation efficiency (SFE, pink). *Centre and right-hand panels:* Density-temperature phase diagrams for the smoothest early type galaxy ($M_* = 10^{11}{\rm M}_\odot$, centre) and the Milky Way-like galaxy simulation (right). Dashed lines delineate the regions of phase space corresponding to the bar-plot in the left-hand panel. The molecular hydrogen mass is subtracted from each of these phase-space regions to produce the bar plot.

thickness and combine separate gas and stellar contributions to the dispersion relation, while Romeo & Falstad (2013) additionally consider separate contributions from the molecular, atomic and ionised gas phases. The solid and dashed lines in Figure 7 show the stellar and gaseous Toomre Q parameters $Q_* = \kappa\sigma_*/3.36G\Sigma_*$ and $Q_{\rm gas} = \kappa\sigma_{\rm gas}/\pi G\Sigma_{\rm gas}$, respectively, where κ is the epicyclic frequency, σ_* and $\sigma_{\rm gas}$ are the stellar and gas velocity dispersions (shown in the centre row of panels), and Σ_* and $\Sigma_{\rm gas}$ are the stellar and gas surface densities (shown in the lower row of panels). The elevated disk stability in the ETGs is driven primarily by the stellar contribution to the Toomre Q parameter: though the gas and stellar velocity dispersions in the ETGs are actually lower than those in the outer Milky Way, and the gas and stellar surface densities are comparable, compact stellar bulges in the four ETGs drive the level of shear κ up by around an order of magnitude.

Comparing Figure 7 to Figures 4 and 5, we can conclude that the Toomre stability of the simulated gas disks drives the clumpiness of the interstellar medium, with lower Toomre Q parameters associated with clumpier morphologies, larger voids in the gas distribution, and puffier gas disks (larger outflows).

4.2. *Galactic outflows and supernova clustering*

Figure 8 shows the total galactic star formation rate (SFR, top panel), the rate of gas outflow ($\dot{M}_{\rm out}$, centre panel) and the mass-loading η of the galactic outflows in each of our simulated galaxies, as a function of the simulation time after each disk has reached a state of dynamical equilibrium. The outflow rates are calculated as the total momentum of the gas moving away from the disk, summed over two planar slabs of thickness 500 pc, located at ±1 kpc above and below the galactic disk. The mass-loading divides this outflow rate by the star formation rate.

The strength and mass-loading of the outflows displays a marked increase with a corresponding decrease in the level of gravitational stability shown in the top row of panels in Figure 7. That is, the ETG simulations have galactic outflows that are 3-4 orders of magnitude weaker than those in the Milky Way-like and NGC 300-like simulations. The Milky Way-like galaxy, with the lowest Toomre Q stability parameter, has the strongest galactic outflows. Figure 9 demonstrates that the outflow strength and mass-loading in our simulations is directly correlated with the level of supernova clustering in each, in agreement with recent numerical results (Fielding et al. 2018; Smith et al. 2020; Jeffreson et al. 2021). Each solid line represents the two-point correlation function $\xi(\Delta)$ of supernova explosions occurring throughout each simulation. If $\xi > 1$, then the supernovae are *more clustered* than would be expected for Poisson (uniform) distribution of objects across the galactic mid-plane; if $\xi < 1$ then they are *less clustered*. The supernovae in the main sequence galaxy simulations display much stronger clustering on all scales than do the ETG simulations (up to an order of magnitude in ξ). The Milky Way-like and NGC 300-like simulations display substantial supernova

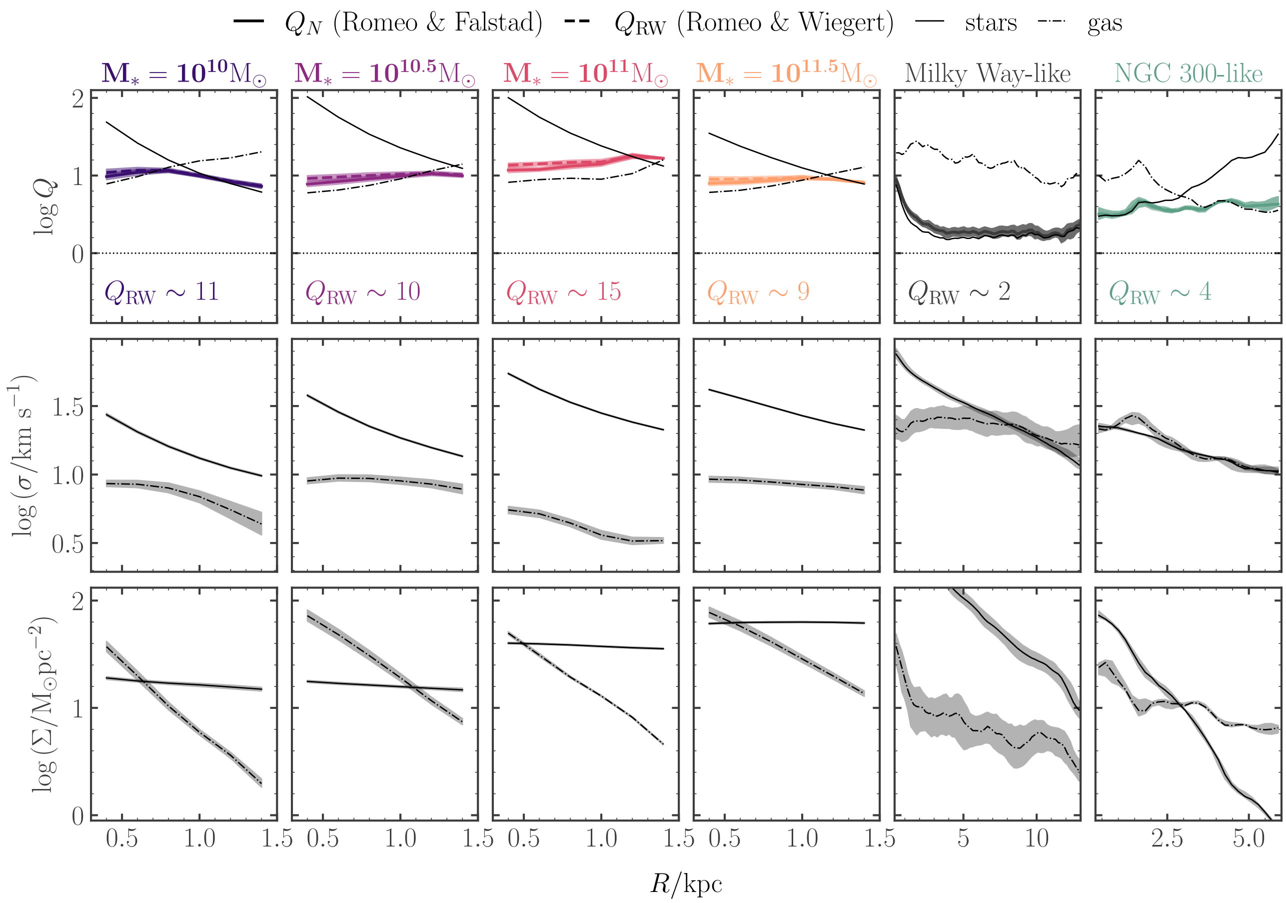

Figure 7. The median Toomre Q parameter (top panels), gas and stellar velocity dispersion (centre panels), and gas and stellar surface density (lower panels) as a function of galactocentric radius for the six galaxies in our sample. Shaded regions represent interquartile ranges over azimuthal angle and simulation time. The Toomre Q parameters of the early type galaxies are much higher than those of the main sequence (Milky Way-like and NGC 300-like) galaxies.

clustering at all scales below $\Delta \sim 100$ pc, while the ETG simulations display supernova clustering only on much smaller scales, below $\Delta \sim 25$ pc.

Figure 10 links this level of supernova clustering to the depletion times, densities (and thus free-fall times) of the most massive star-forming giant molecular clouds, in which the majority of massive clusters form. Jeffreson et al. (2023) have already showed that the high-mass population of molecular clouds is responsible for nearly all of the supernova clustering on small scales in our NGC 300-like simulation (see their Figure 14). In this work, we identify molecular clouds as closed contours in the molecular gas surface density at a threshold of $\Sigma_{\rm H_2} = 30\ \mathrm{M_\odot pc^{-2}}$. The masses and volume densities reported in the figure are molecular gas masses and densities.

Panel (a) of Figure 10 shows the star formation rate per cloud as a function of mass, demonstrating that the majority of star formation in our simulations occurs in the most massive molecular clouds ($> 10^6\ \mathrm{M_\odot}$), in agreement with observations (e.g. Murray & Rahman 2010). Panel (b) shows that the molecular gas depletion time is an order of magnitude higher in the massive clouds of the ETG (high-Q) disks than it is in the high-mass clouds of the main sequence (low-Q) galaxy disks, associated with a molecular gas volume density that is over an order of magnitude lower (panel c). This lower volume density corresponds to a factor ~ 4 higher cloud free-fall time $\tau_{\rm ff,cl}$ for the ETGs, in accordance with the expectation that $\tau_{\rm ff,cl} \propto Q$ in axisymmetric disks in hydrostatic equilibrium (e.g. Krumholz & McKee 2005; Jeffreson & Kruijssen 2018). Thus the level of supernova clustering is driven down in the ETGs by (1) an increase in size of the most massive molecular clouds, and (2) a decrease in the cloud star formation efficiency, driven by an increase in virial parameter (see Equation 3). Panel (d) shows only slightly higher frequencies of massive molecular clouds in the main sequence galaxies, indicating that the properties of these massive GMCs (not their number) is not the main driver of supernova clustering.

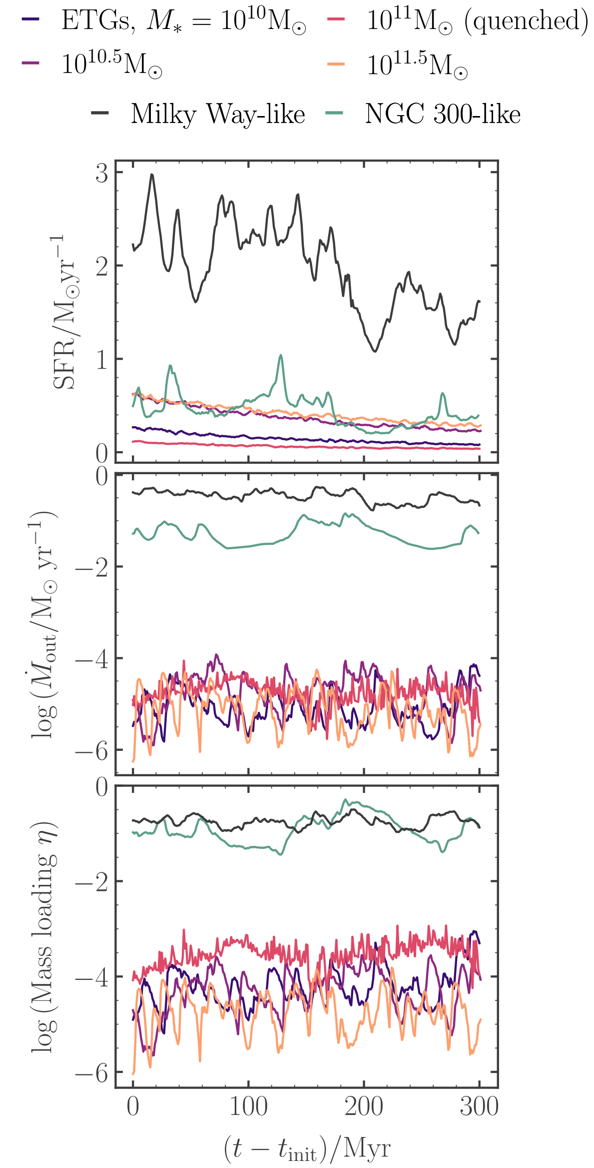

Figure 8. Global galactic star formation rate (upper panels), gas outflow rate (central panels) and mass-loading of outflows (lower panels) as a function of the simulation time after which each gas disc has reached a state of dynamical equilibrium (100 Myr onwards for the ETG simulations, 300 Myr onwards for the Milky Way-like simulation, and 500 Myr onwards for the NGC 300-like simulation).

We therefore deduce that large differences in the strength of galactic outflows between main sequence and quenched galactic environments are driven by large differences in the levels of supernova clustering. The level of supernova clustering is associated with the level of gas disk gravitational stability, which sets the free-fall times within the most massive molecular clouds. High levels of disc stability in the ETGs therefore produce very smooth gas discs with very small feedback-driven voids and outflows as observed by (Davis et al. 2022) and reproduced in our Figure 5.

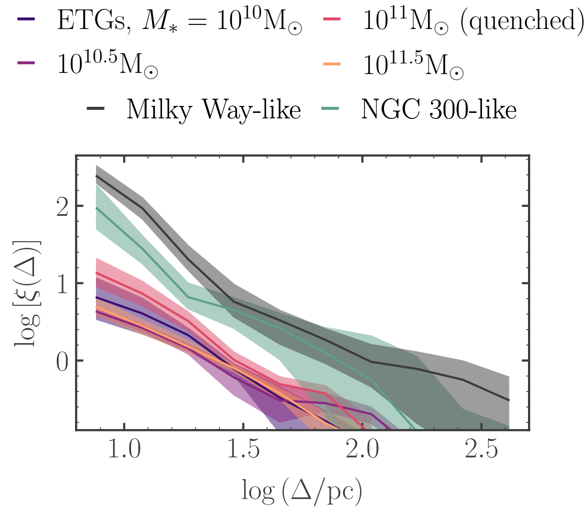

Figure 9. The two-point correlation function $\xi(\Delta)$ for supernova explosions (quantifying the degree of supernova clustering) as a function of their separation Δ over time intervals of 1 Myr, averaged over all times throughout each simulation (solid lines). The shaded regions give the interquartile ranges over these times. The level of supernova clustering is higher on all scales in the Milky Way-like and NGC 300-like simulations, relative to the early type galaxy simulations.

Finally, we note that the giant molecular clouds in the quenched ETG (pink lines in Figure 10) have lower densities than in the other three ETGs, and contain almost no star formation, despite the fact that this disk has only a marginally-higher value of the Toomre Q parameter. We will explore this phenomenon in greater detail in Section 6.

4.3. *The equation of state (mid-plane gas density vs. mid-plane pressure)*

The equation of state relating the total turbulent plus thermal mid-plane pressure P_{tot} and mid-plane density ρ of the cool-warm ($T < 10^4$ K) gas depends on the turbulent velocity dispersion σ of the gas as $P_{\mathrm{tot}} \sim n_{\mathrm{H}} m_{\mathrm{p}}(\sigma^2_{\mathrm{turb}} + c_s^2)$, and therefore on any physical processes that affect the driving turbulence. Figure 4.2 shows the equation of state for our galaxy simulation suite, with each filled data point representing one radial annulus of width 500 pc and separation 200 pc. Isotherms are given by grey dotted lines.

The ETG simulations in our sample have very different equations of state and much lower temperatures than our Milky Way-like and NGC 300-like simulations.The lowest temperature of $\sim$ 1000 K is found for the gas in the morphologically-quenched galaxy. This is con-

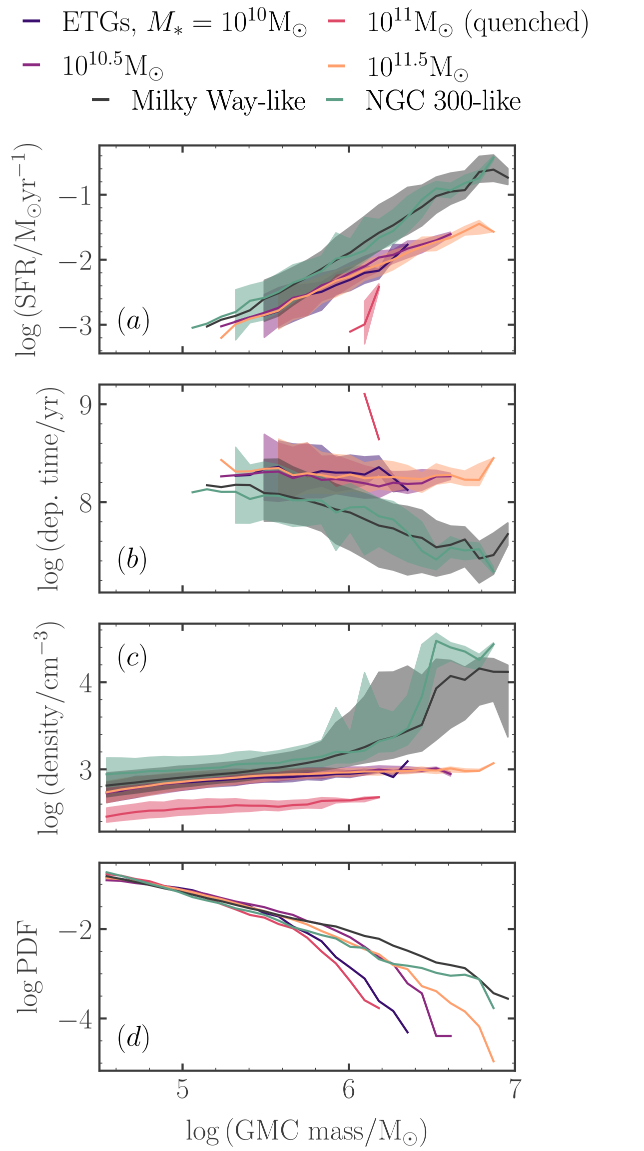

Figure 10. Molecular cloud star formation rate (a, SFR), molecular gas depletion time (b), and molecular gas volume density (c) as a function of the molecular cloud mass, the distribution of which is shown in panel (d). Solid lines represent median values over all simulation times, while shaded regions represent interquartile ranges. The absence of values in the upper two panels indicates that the median or first quartile star formation rate at these molecular cloud masses is zero.

sistent with the much larger cold gas fractions in these disks (Figure 6). It is also consistent with the much lower levels of supernova clustering, and with the reduced strength of galactic outflows (Figures 8 and 9), driven down by rotationally-induced gravitational stability.

That is, less supernova clustering means a smaller quantity of momentum injected per unit star formation, leading to a lower turbulent velocity dispersion σ for the ETG simulations, as reported in the middle row of Figure 7. However, the mid-plane pressure of each disk seeks to maintain a state of hydrostatic equilibrium, and thus n_{H} increases relative to the mid-plane pressure. The ETG disks are therefore shifted to the right in the n_{H} vs. P_{tot} plane, corresponding to a factor 3 drop in the turbulent velocity dispersion, lowered disk scale-heights, and higher molecular fractions.

The thick dashed line in Figure 4.2 corresponds to the best fit to the equation of state from the TIGRESS simulations (Ostriker & Kim 2022). The TIGRESS equation of state is in very good agreement with our main sequence galaxy simulations, but not with our ETG simulations. This is consistent with the galactic angular momentum in the TIGRESS simulations, as reported in Kim et al. (2020): their maximum value is $\Omega = 0.1\ \mathrm{Myr}^{-1}$, consistent with the rotation curves in our Milky Way-like and NGC 300-like galaxies (see Figure 3). By contrast, our ETG simulations have angular momenta between $\Omega \sim 0.1$ and $\Omega \sim 3$. We therefore expect the level of rotational support, the gravitational stability, the level of supernova clustering and the equation of state from TIGRESS to agree with our main sequence simulations, but not with our ETG simulations.

Because the energy and momentum injection due to stellar feedback cannot be resolved in cosmological simulations, the equation of state must be modelled via a subgrid prescription, similarly to the SFR. The equation of state used in the Illustris simulations (Springel & Hernquist 2003) is given by the thick grey line in Figure 4.2. A preferable fit to the star-forming gas in main sequence galaxies can be obtained by fitting directly to high resolution simulations, such as GalactISM or TIGRESS. However, this will not capture the substantial differences in gas disk temperature associated with rotationally-stabilised ETG disks.

Despite this, comparing Figures 3 and 4.2 demonstrates that the offset in turbulent velocity dispersion between the main sequence galaxies and ETGs is driven by the galactic rotation curve Ω. It may therefore be possible to predict the relationship between P_{tot} and n_{H} within a parameter space that includes Ω.

5. STAR FORMATION REGULATION

Power-law relationships between the star formation rate surface density Σ_{SFR} and other large-scale properties of galaxies provide important constraints for theories of galactic star formation, and function as subgrid models for star formation in cosmological simulations,

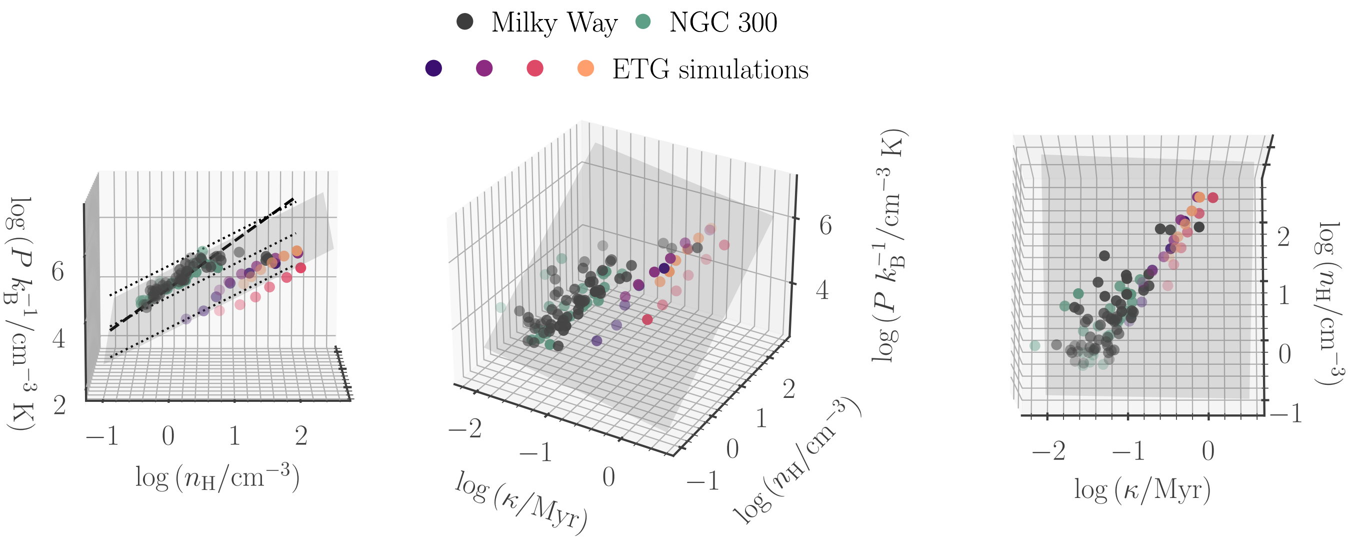

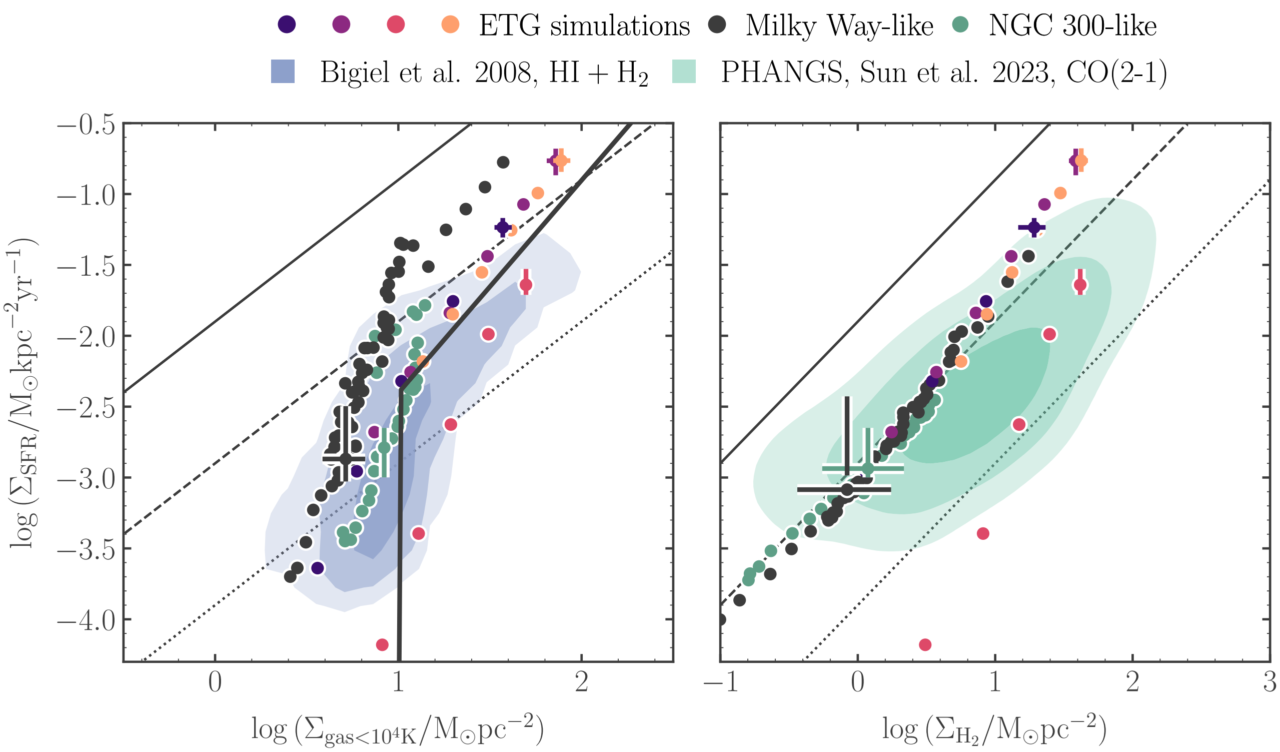

Figure 11. Star formation rate surface density $\Sigma_{\rm SFR}$ as a function of the $< 10^4$ K gas surface density $\Sigma_{\rm gas<10^4K}$ (left) and as a function of the molecular gas surface density $\Sigma_{\rm H_2}$ (right). Solid, dashed and dotted lines represent depletion times of 10^8, 10^9 and 10^{10} Gyr, respectively. Filled data points represent median values over time for each simulated galaxy, measured within overlapping radial annuli of width 500 pc. For visual clarity, the corresponding interquartile ranges are shown at just one representative radius in each galaxy. The thick black line represents the star formation model adopted in Illustris-TNG (see Section 5.1). The blue and green contours represent the 40%-80%-95% levels of the observed observed galaxy samples from Bigiel et al. (2008) and Sun et al. (2023), respectively.

where the detailed physics of the interstellar medium cannot be resolved. In this section we compare powerlaws of the star formation surface density $\Sigma_{\rm SFR}$ vs. the gas surface density $\Sigma_{\rm gas}$, and of $\Sigma_{\rm SFR}$ with the interstellar medium weight $\mathcal{W}$ (alternatively the mid-plane pressure $P_{\rm tot}$).

5.1. *Gas surface density vs. star formation rate surface density*

The most common subgrid model for star formation in cosmological simulations sets a depletion time of $\tau_{\rm dep} = \tau^{-1}_{\rm dep,0}(\rho_{\rm gas}/\rho_{\rm thresh})^{0.5}$, where $\rho_{\rm gas}$ is the volume density of the gas, $\rho_{\rm thresh}$ is the density above which star formation is allowed to occur, and $\tau_{\rm dep,0}$ is the gas depletion time at this threshold. The resulting inverse proportionality between the star formation rate (SFR) and the gas free-fall time $\sqrt{3\pi/32G\rho_{\rm gas}}$ is in agreement with a sample of 21 observed spiral galaxies at low redshift from Kennicutt (1998), which follow the powerlaw $\Sigma_{\rm SFR} \propto \Sigma^{1.5}_{\rm gas}$ with $\Sigma_{\rm gas} > 10~{\rm M_\odot pc^{-2}}$ averaged across galactic disks (the 'Schmidt-Kennicutt relation'). The thick black line in the left-hand panel of Figure 11 represents this powerlaw, with the depletion time of 2.2 Gyr at $\Sigma_{\rm gas} > 10~{\rm M_\odot pc^{-2}}$ that is used in Illustris-TNG (Springel & Hernquist 2003; Vogelsberger et al. 2013), and is qualitatively very similar to the relationship used to calibrate star formation models in other large cosmological simulations, including MUFASA Davé et al. (2016), SIMBA (Davé et al. 2019) and EAGLE (Schaye et al. 2015).

The left-hand panel of Figure 11 demonstrates that this relationship between $\Sigma_{\rm SFR}$ and $\Sigma_{\rm gas}$ provides a reasonable approximation to the median resolved star formation rate across our high-resolution galaxy simulations (filled data points), with two major caveats. Firstly, there is nearly an order of magnitude of galaxy-to-galaxy variation in the normalisation of $\Sigma_{\rm SFR}$ with $\Sigma_{\rm gas}$ in our simulations, which cannot be captured by a single function. Secondly, the cut-off at $\Sigma_{\rm gas} = 10~{\rm M_\odot pc^{-2}}$ ignores the star formation occurring in the lower-density gas at large galactocentric radii, with potential consequences for the strength of galactic outflows in the galaxy outskirts. This gas with $\Sigma_{{\rm gas}<10^4{\rm K}} < 10~{\rm M_\odot pc^{-2}}$ accounts for most of the gas outside galactocentric radii of 3 kpc in the Milky Way-like and NGC 300-like disks, in agreement with the observed molecular and atomic gas distribution across a sample of 18 nearby spiral galaxies at 750 pc resolution (Bigiel et al. 2008).

By contrast, the right-hand panel of Figure 11 shows that the relationship between the molecular gas surface density $\Sigma_{\rm H_2}$ and the star formation rate surface density is much easier to capture with a single powerlaw (for all but the morphologically-quenched ETG, to which we will return in Section 6). Though a slight decrease in the molecular gas depletion time is visible for the ETG simulations, the trend can be well modelled in general by a powerlaw of the form $\Sigma_{\rm SFR} \propto \Sigma_{\rm H_2}$ with a depletion time of around 1 Gyr, in agreement with observations of the molecular gas distribution across a sample of 80 nearby galaxies at 1.5 kpc resolution (Sun et al. 2023, green contours). That is, with the exception of the morphologically-quenched galaxy, the efficiency of star formation in the molecular gas is roughly constant at 10 per cent across our galaxy sample, across three orders of magnitude in the molecular gas surface density.

Ideally, the relationship between $\Sigma_{\rm H_2}$ and $\Sigma_{\rm SFR}$ would be used to model star formation in cosmological volume simulations, however the resolution requirements for modelling the molecular gas reservoir ($\sim 10^3{\rm M_\odot}$) are four orders of magnitude out-of-reach for a cosmological box the same size as Illustris TNG-300 ($\sim 10^7{\rm M_\odot}$). Fortunately, as we will see in the next subsection, the mid-plane pressure is an equally good predictor of the star formation rate surface density across a wide range of galaxy environments including both main sequence and quenched/low gas-fraction galaxies.

5.2. *ISM weight vs. star formation rate surface density*

Recent analyses of a large sample of main sequence galaxies from the PHANGS-ALMA sample (Leroy et al. 2021) have demonstrated a close correlation between the kpc-scale mid-plane pressure $P_{\rm tot}$ of gas disks in hydrostatic equilibrium and the galactic star formation rate surface density $\Sigma_{\rm SFR}$ (Sun et al. 2023), as well as the fraction of dense and self-gravitating molecular gas (Sun et al. 2020). Such a relationship between the star formation rate and the mid-plane pressure is a central tenet of 'pressure-regulated' theories of star formation (e.g. Thompson et al. 2005; Ostriker et al. 2010; Ostriker & Shetty 2011; Hopkins et al. 2011). These theories posit that the the star formation rate adjusts so that the vertical gas disk pressure produced by feedback-driven turbulence and thermal energy is in hydrostatic balance with the weight of the interstellar medium. The correlation between $P_{\rm tot}$ and $\Sigma_{\rm SFR}$ is reproduced in stratefied boxes representing a range of observable galactic environments (e.g. Kim & Ostriker 2015; Ostriker & Kim 2022), but has not yet been investigated in high-resolution isolated galaxy simulations.

The left-hand side of Figure 12 shows the relationship between $P_{\rm tot}$ and $\Sigma_{\rm SFR}$ within radial annuli across our simulated galaxies. Our method for calculating the total (turbulent plus thermal) mid-plane pressure is described

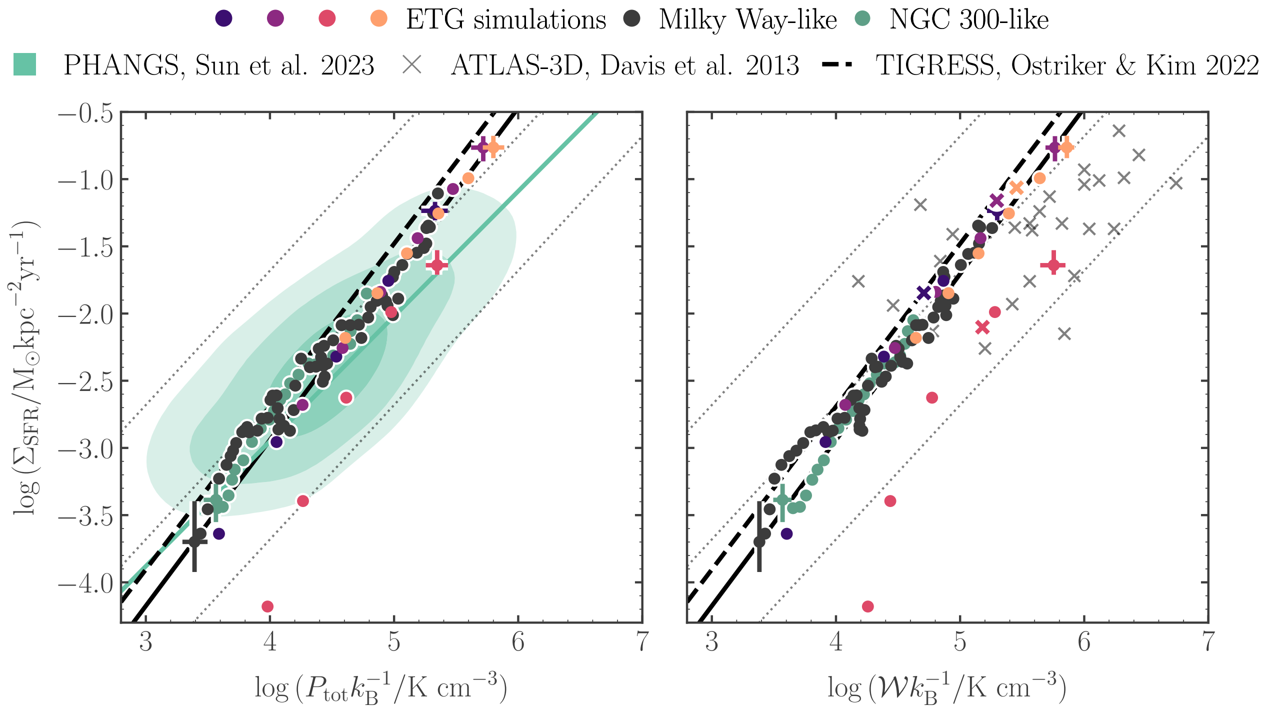

Figure 12. Star formation rate surface density $\Sigma_{\rm SFR}$ as a function of the total mid-plane pressure $P_{\rm tot}$ (left) and as a function of the interstellar medium weight $\mathcal{W}$ (right, see Section 5.2). Solid dashed and dotted lines represent constant ratios of $\Sigma_{\rm SFR}/P_{\rm tot} = 10^2$, 10^3 and 10^4 km s^{-1}. Filled data points represent median values over time for each simulated galaxy, measured within overlapping radial annuli of width 500 pc. For visual clarity, the corresponding interquartile ranges are shown at just one representative radius in each galaxy. The thick black line represents the best linear regression fit to these data points, excluding the morphologically-quenched galaxy (hot pink). The thick dashed line represents the corresponding best fit from the TIGRESS simulations Ostriker & Kim (2022). The green contours represent the 40%-80%-95% levels of the observed galaxy sample from Sun et al. (2023).

in Appendix B. The best fit to these data (thick black line), excluding the morphologically-quenched galaxy (pink data points) is given by

$$\log_{10}\left(\frac{\Sigma_{\rm SFR}}{{\rm M_\odot kpc^{-2}yr^{-1}}}\right) = 1.235\log\left(\frac{P_{\rm tot}k_{\rm B}^{-1}}{{\rm cm^{-3}K}}\right) - 7.86, \quad (4)$$

and shows good agreement with the observed relationship between $\Sigma_{\rm SFR}$ with $P_{\rm tot}$ across a sample of 80 nearby galaxies at 1.5 kpc scales (Sun et al. 2023), in which star formation rates are traced by Hα + 22μm emission and gas is traced by CO(2-1) emission, with a CO(2-1)/(1-0) conversion factor of 0.65 and an CO-to-H_2 conversion factor set according to Bolatto et al. (2013). The slightly steeper slope in our simulations may be due to differences in the gas and star formation reservoirs we have analysed and those traced by CO and Hα emission in the observations, or due to a number of numerical effects.

For example, we may slightly under-estimate the momentum injected by stellar feedback in our simulations at high mid-plane pressures, or under-estimate the extent to which turbulence is driven by processes other than stellar feedback, such as radial mass transport (discussed in the next subsection). Both of these effects would reduce the turbulent pressure provided per unit of star formation. We obtain a similar slope to that of the TIGRESS simulations, with a slightly reduced normalisation factor, attributable again to the different feedback model used in our simulations, or to the presence of radial mass transport, which is not present in stratefied box simulations.

Excluding the morphologically-quenched galaxy, the correlation between $\Sigma_{\rm SFR}$ and $P_{\rm tot}$ in our simulations is tight, indicating that the mid-plane pressure is a key regulator of the molecular gas surface density $\Sigma_{\rm H_2}$ and consequently of the star formation rate, in line with theoretical expectations. The right-hand panel of Figure 12 additionally demonstrates that the mid-plane pressure can be approximated by the interstellar medium weight $\mathcal{W}$ across our simulation suite, such that

$$P_{\rm tot} \sim \mathcal{W} = \int_0^{z_{\rm max}} \rho_{\rm gas}(z)\frac{\partial\Phi}{\partial z}{\rm d}z, \quad (5)$$

where $z_{\rm max}$ is the maximum extent of the gas disk, $\rho_{\rm gas}$ is the gas volume density, and Φ is the gravitational poten-

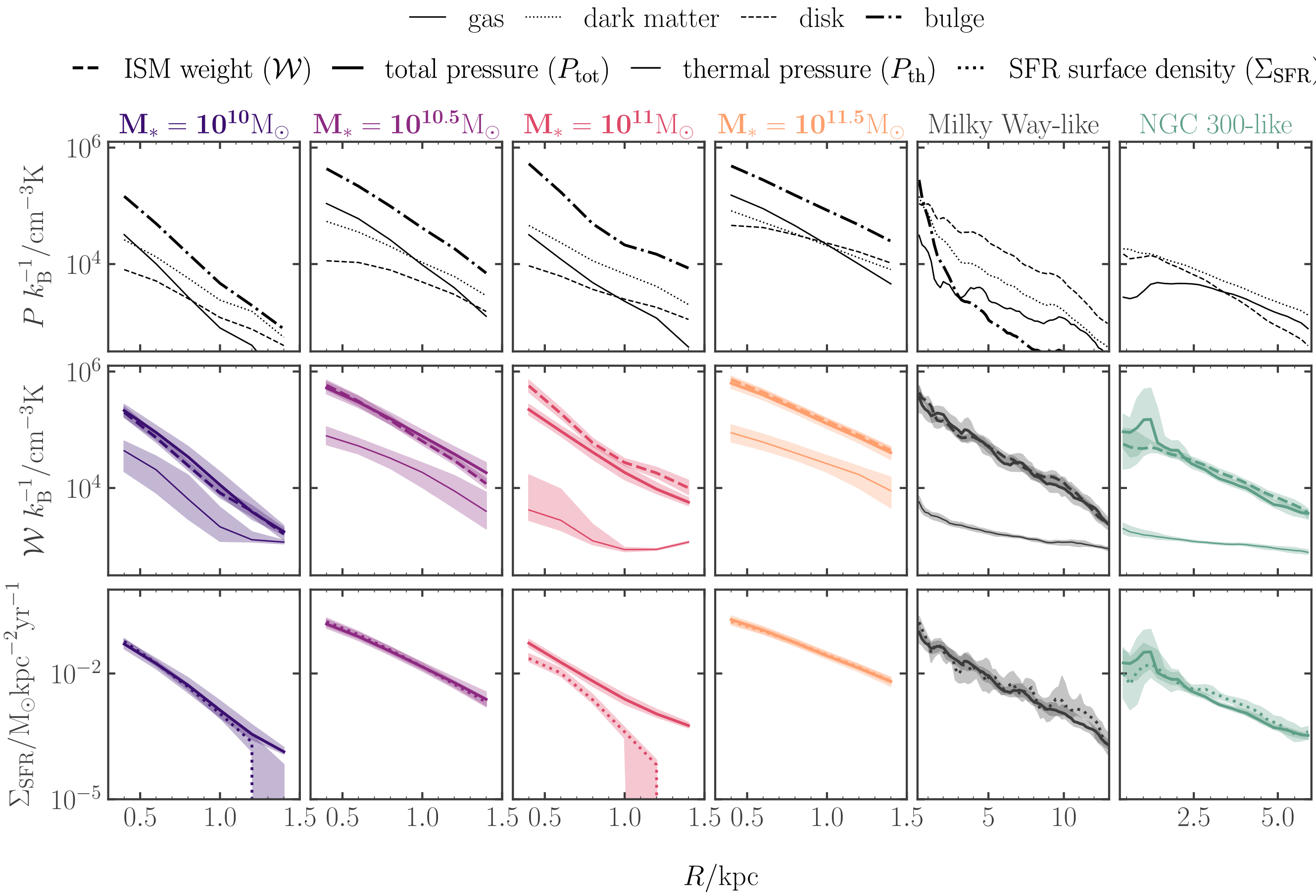

Figure 13. *Top:* The ISM weight $\mathcal{W}$ due to each component of the gravitational potential, as a function of the galactocentric radius. *Centre:* Comparison of the total mid-plane pressure (solid lines) and the total ISM weight (dashed lines), along with median values of the thermal mid-plane pressure (thin lines) as a function of galactocentric radius. *Top:* Comparison of the true star formation rate surface density $\Sigma_{\rm SFR}$ (dotted lines) and the star formation rate surface density predicted by Equation 4. All values are median values over time, and all shaded areas are the corresponding interquartile ranges.

tial due to the entire distribution of gas, stars and dark matter. Our method for calculating $\mathcal{W}$ using the three-dimensional distribution of gas, stars and dark matter in our simulation is given in Appendix B. Figure 12 therefore demonstrates that, averaged over time, the gas disks of our simulated galaxies are in hydrostatic equilibrium. Because the ISM weight $\mathcal{W}$ can be calculated in terms of the large-scale properties of galaxies (see Section 3 of Hassan et al. 2023, for details), Equation (4) can therefore be used to model star formation in cosmological simulations, so long as the assumption of hydrostatic equilibrium holds.

In Figure 13, we show the same data as is presented in Figure 12, but in greater detail for each simulated galaxy, with interquartile ranges over time and azimuthal angle at each galactocentric radius (transparent shaded regions). The separate contributions to the ISM weight $\mathcal{W}$ made by the gas disk (solid lines), dark matter halo (dotted lines), stellar disk (dashed lines) and stellar bulge (thick dot-dashed lines) are shown in the top row, clearly demonstrating that $\mathcal{W}$ is dominated by the stellar bulge in the ETG simulations, by the stellar disk in the Milky Way-like simulation, and by the disk and dark matter halo in the NGC 300-like simulation. In the centre row we show that a state of hydrostatic equilibrium is maintained in all but the quenched ETG simulation, with close overlap between the mid-plane pressure (thick solid lines) and the ISM weight (thick dashed lines). The thermal pressure (thin lines) is also shown, for comparison. Finally, the bottom row shows the correspondence between the measured star formation rate surface density $\Sigma_{\rm SFR}$ for each simulation as a function of galactocentric radius and the value predicted via Equation (4). The same powerlaw relation between $P_{\rm tot}$ and $\Sigma_{\rm SFR}$ manifestly holds across all five galaxies.

We therefore find that Equation (4) may hold promise as an improved, predictive subgrid model for star formation in cosmological sim-

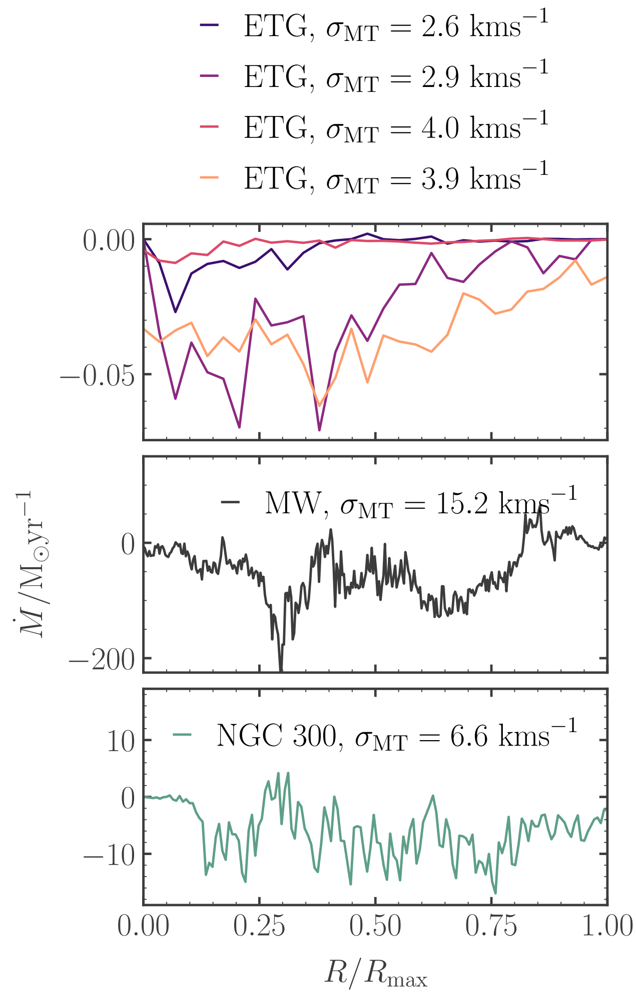

Figure 14. The median value over time of the radial mass flux in each of our simulations, as a function of the scaled galactocentric radius (0 represents the smallest radius analysed, which is 0.3 kpc for all galaxies, and 1 represents the largest radius analysed). Negative values indicate that the net direction of mass transport is inward, over the simulation times analysed. The values of $\sigma_{\rm MT}$ in the legend represent the approximation for the turbulent velocity dispersion produced by inward radial mass transport in the absence of stellar feedback, computed via Equation (9) for each simulation.

ulations, across a range of main sequence and quenched galaxy environments. This model provides a prediction for the star formation rate based on the theoretical prediction of Ostriker & Kim (2022), rather than a fit to a relatively small sample of nearby main sequence spirals, as is the current state-of-the-art in cosmological simulations (left-hand side of Figure 11).

5.3. *The morphologically-quenched galaxy*

Figure 12 demonstrates that the morphologically-quenched galaxy simulation lies around seven or eight times offset in the value of $\Sigma_{\rm SFR}/P_{\rm tot}$, relative to all five of the other galaxy simulations. However, its inner regions are not inconsistent with the spread of the observed main sequence observations, given by the green contours in the left-hand panel. We may also estimate the positions of the ATLAS-3D galaxies in the plane of ISM weight $\mathcal{W}$ vs. the star formation rate surface density $\Sigma_{\rm SFR}$ (grey crosses, right-hand panel).

We have approximated the ISM weight for the ATLAS-3D sample by making a number of geometrical approximations regarding the gas disc, stellar bulge, and dark matter halo. The median disc-to-bulge ratio in the galaxies is zero, such that

$$\mathcal{W} = \mathcal{W}_{\rm g} + \mathcal{W}_{*,\rm b} + \mathcal{W}_{\rm dm}, \tag{6}$$

where $\mathcal{W}_{\rm g}$ is the weight of the gas due to its own gravitational potential, $\mathcal{W}_{*,\rm b}$ is the weight due to the potential associated with the stellar bulge, and dm is the weight due to the potential associated with the dark matter halo. Assuming a plane-parallel geometry for the gas,

$$\mathcal{W}_{\rm g} = \frac{\pi G \Sigma_{\rm g}}{2}, \tag{7}$$

where $\Sigma_{\rm g}$ is the gas surface density. Both the stellar bulge and dark matter components have spherical distributions, such that their combined weight can be approximated as

$$\mathcal{W}_{*,\rm b} + \mathcal{W}_{\rm dm} = \zeta \Sigma_{\rm g} (\Omega_{*,\rm b} + \Omega_{\rm dm}) h_{\rm g}, \tag{8}$$

where $h_{\rm g}$ is the gas disc scale-height, and we have assumed that $h_{\rm g}$ is much smaller than the scale-lengths of both the bulge and the halo, with $\zeta \sim 1/3$ (see Ostriker & Shetty 2011). For the ATLAS-3D galaxies, we assume a Plummer profile for the bulge and an NFW profile for the halo, as in our simulations, and calculate $\Omega_{*,\rm b}$ and $\Omega_{\rm dm}$ from the measured values of the stellar half-light radius $R_{*,1/2}$ and the virial halo mass M_{200}, as shown in Figure 1. In addition to these ATLAS-3D values of $\mathcal{W}$ and $\Sigma_{\rm SFR}$ (grey crosses), we show the galaxy-averaged values for our simulated ETGs as coloured crosses (filled circles represent values within radiall annuli on 500 pc scales).

Figure 12 therefore shows, both for the simulated and observed ETGs, which show good agreement, a larger scatter down to lower values of $\Sigma_{\rm SFR}/\mathcal{W}$ (equivalently $\Sigma_{\rm SFR}/P_{\rm tot}$ if hydrostatic equilibrium is assumed) than do the simulated and observed main sequence galaxies. This is in line with expectations if a fraction of the observed ETGs are morphologically-quenched in the same way as in our simulated ETG of stellar mass $M_* = 10^{11}{\rm M}_\odot$. In this simulation, the suppressed star

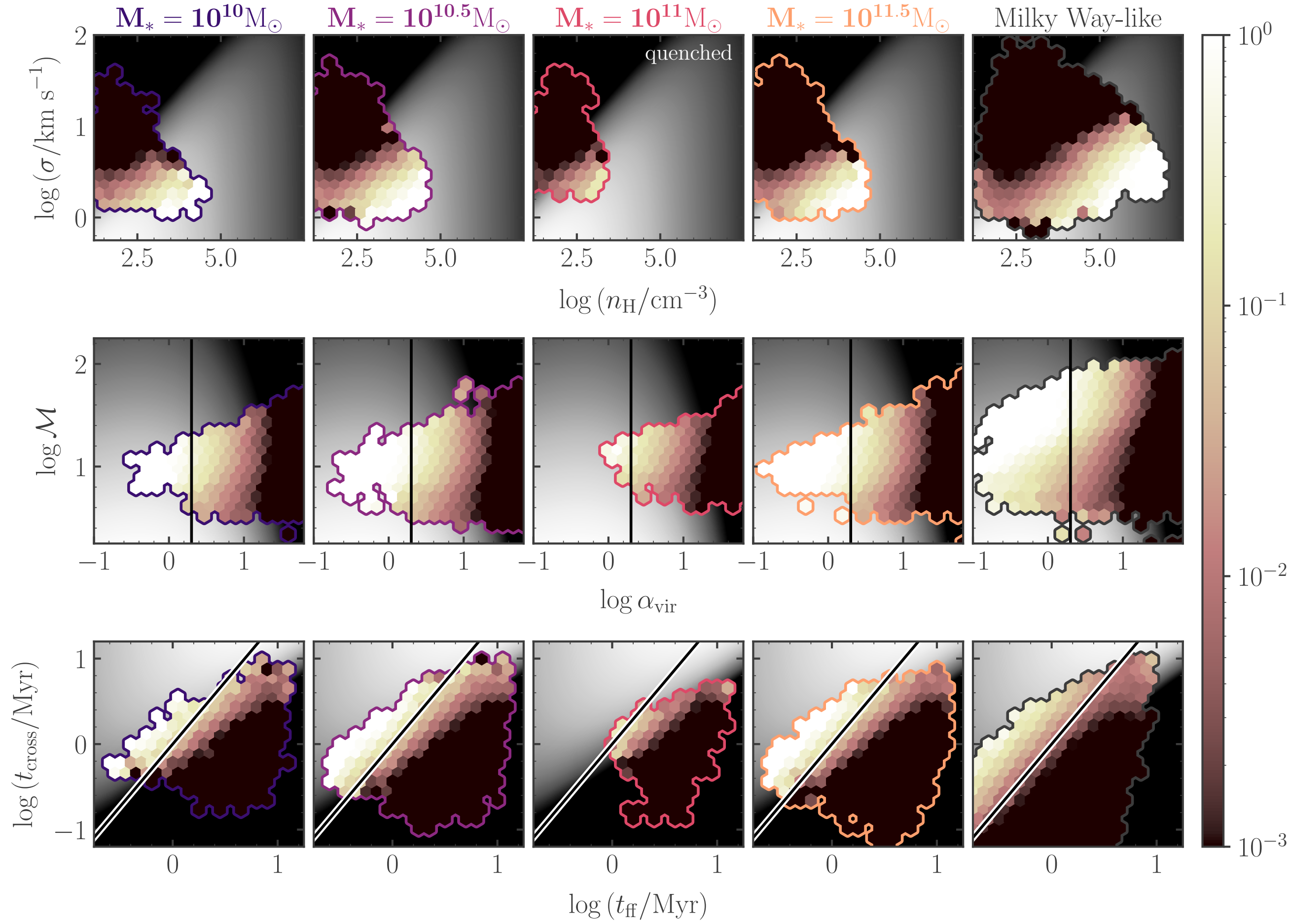

Figure 15. Star formation efficiencies (pink contours) for the star-forming gas in five of our simulations (see Section 6) as a function of the gas volume density n_H and velocity dispersion σ (top), the virial parameter α_vir and Mach number $\mathcal{M}$ (centre) and the free-fall time t_ff and crossing time t_cross (bottom). Black lines divide gravitationally bound and unbound gas populations: $\alpha_\mathrm{vir} = 2$ (centre) and $t_\mathrm{ff} = t_\mathrm{cross}$ (bottom). Grey contours give the corresponding analytic predictions for the star formation efficiency according to Equation 3 at a fixed length-scale of 20 pc.

formation results in a reduction in the turbulent velocity dispersion (middle row, Figure 7), which prevents the galaxy from reaching equality between its ISM weight and mid-plane pressure. It is thus out of hydrostatic equilibrium, as shown in the middle row of Figure 13.

5.4. *The source of turbulent pressure*

Comparing the turbulent velocity dispersion of the gas in Figure 7 with the star formation rate surface density Σ_SFR in Figure 13, it is clear that stellar feedback cannot be the only source of turbulence in the morphologically-quenched galaxy. While Σ_SFR drops steeply outside galactocentric radii of 1 kpc, the turbulent velocity dispersion flattens to a value of ~ 3 km/s.

An alternative source of turbulence is inward radial mass transport within the reservoir of cool-warm gas (Krumholz & Burkert 2010; Krumholz et al. 2018). As gas flows down the galactic gravitational potential, it loses gravitational potential energy, which is converted to kinetic energy in the form of turbulent eddies. Such radial mass transport has been shown to sustain velocity dispersions of ~ 10 km/s in isolated galaxy disks without any form of stellar feedback (Goldbaum et al. 2015). The maximum turbulent velocity dispersion σ_MT that can be sustained by mass transport in the absence of stellar feedback can be approximated by equating the potential energy lost per unit time due to flowing down the gravitational potential well, to the rate of turbulent kinetic energy dissipation, such that

$$\eta\sigma_\mathrm{MT}^2\Omega \sim \frac{\mathrm{d}\Phi}{\mathrm{d}R}\overline{v}_R, \tag{9}$$

where $\eta \sim 1.5$ is the coefficient of turbulent dissipation, Ω is the galactic orbital angular velocity, $\mathrm{d}\Phi/\mathrm{d}R$ is the radial gradient of the gravitational potential, and $\overline{v_\mathrm{R}}$ is the time-averaged inward radial velocity of warm-cold gas in the disc.

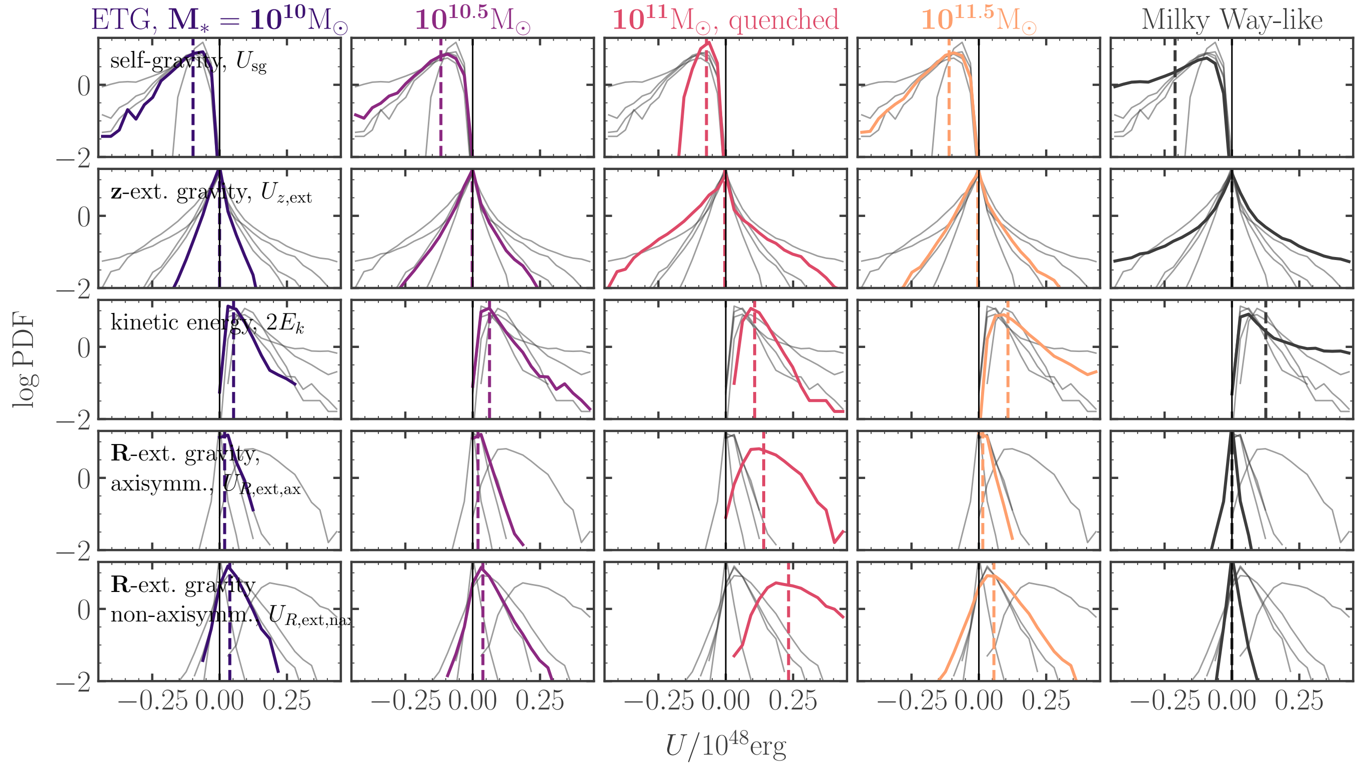

Figure 16. Probability density functions (PDFs) for the five contributions to the energy budget of star-forming overdensities in five of our simulations, at a single snap-shot in time. These are the energy $U_{\rm sg}$ due to the self-gravity of the overdensities (top), the energy $U_{z,\rm ext}$ due to the external galactic potential in the galactic z-direction (second-top), the turbulent and thermal internal kinetic energy $2E_k$ (middle), and the axisymmetric and non-axisymmetric parts of the energy $U_{R,\rm ext}$ due to the external galactic potential within the galactic mid-plane. Thin black lines delineate $U = 0$, and separate compressive ($U < 0$) from expansive ($U > 0$) energy terms. The PDF for one simulation is highlighted in colour in each column. Dashed lines represent median values. Only the values for overdensities with average star formation efficiencies SFE > 0.01 are shown.

In Figure 14, we show the median rate of inward radial mass transport $\dot{M}$ over time, as a function of galactocentric radius for each of our simulated galaxies. We calculate this as the mass flux $\dot{M}(R) = 2\pi R \int \rho(R,z) v_R(R,z) {\rm d}z$ across the centres of annular radial bins of width 40 pc, where the gas cells in the bin at R have densities $\rho(R,z)$ and radial velocities $v_R(R,z)$. The average radial velocity over the bin is therefore $\overline{v}_R(R) = \dot{M}(R)/[2\pi R \int \rho(R,z){\rm d}z]$. In the legend we give the values of $\sigma_{\rm MT}$ calculated via Equation (9) for each galaxy. They are approximately equal to the turbulent velocity dispersion values presented in the bottom row of Figure 7, for all simulated galaxies. The value $\sigma_{\rm MT} \sim 4$ km/s for the morphologically-quenched galaxy is higher than the value of 3 km/s seen in the outskirts of the morphologically-quenched galaxy: this may be due to the increased, numerically-augmented, rate of turbulent dissipation η in our simulations, relative to the theoretically-expected value (e.g. Semenov et al. 2022). We conclude that **both stellar feedback and inward mass transport are credible sources of turbulence in our galaxies, with mass transport providing a likely source of the turbulence in the morphologically-quenched ETG at galactocentric radii $R < 1$ kpc.**

6. THE CAUSE OF MORPHOLOGICAL QUENCHING

One galaxy in our simulation suite is an outlier in terms of both star formation rate and star formation efficiency. Its star formation rate is decoupled from the pressure regulation that sets $\Sigma_{\rm SFR}$ across the other five galaxies, and its molecular gas depletion time is ten times longer (10^{10} Gyr). Surprisingly, its level of axisymmetric gravitational stability Q is only 40 per cent higher than the three other early type galaxies, which are not quenched. In the following sub-sections, we investigate the role of non-axisymmetric forces in driving this morphological quenching.

6.1. *A lack of gravitationally-bound gas*

As described in Section 2.2, the star formation efficiency in our simulations is determined by the gravitational boundedness of the gas above a density threshold of $\rho_{\rm thresh} = 100\ {\rm cm}^{-3}$, parametrised by the virial parameter $\alpha_{\rm vir}$. A lower value of the virial parameter results in an exponentially higher efficiency, via Equation 3. The virial parameter is calculated within overdensities surrounding each star-forming gas cell; the scale of each overdensity is determined via a variant of the Sobolev (1960) as the characteristic length-scale for changes in the density of the surrounding gas $L = \rho/|\nabla\rho|$, where $\nabla\rho = \partial\rho/\partial r$ is the density gradient with distance r from the central gas cell. The median radius of these overdensities is ~ 10 pc, and they contain 140 gas cells on average.

Figure 15 shows the average star formation efficiency (pink contours) within these star-forming overdensities, as a function of the volume density $n_{\rm H}$ and velocity dispersion σ (top row), the virial parameter $\alpha_{\rm vir}$ and Mach number $\mathcal{M}$ (centre row) and the gas free-fall and crossing times $t_{\rm ff}$ and $t_{\rm cross}$ (bottom row). Each property is calculated as a weighted average over the gas cells inside L, using a cubic spline kernel (Monaghan 1992). The grey-scale contours in each panel represent the star formation efficiencies that would be calculated via Equation 3 for a fixed length-scale of 20 pc. For readability, we have omitted the NGC 300-like galaxy from this figure, but its star-forming gas has qualitatively similar properties to that of the Milky Way-like galaxy.

Figure 15 demonstrates that a lack of gravitationally-bound gas sets the morphologically-quenched galaxy apart from the other ETGs and the Milky Way-like galaxy. Only a tiny fraction of the gas sits in the region of parameter space with $t_{\rm ff} < t_{\rm cross}$ and $\alpha_{\rm vir} < 2$. This is due both to a higher minimum velocity dispersion σ and to a lower maximum density $n_{\rm H}$ (top row). As a result, while all other galaxies have a substantial fraction of gas with SFE > 0.1, the morphologically-quenched galaxy has almost none, causing the steep drop in SFE in the left-hand panel of Figure 6.

6.2. *Gravitational support on cloud scales*

We have seen in the previous sub-section that suppressed gravitational collapse within the densest gas on scales of around 20 pc is responsible for the morphological quenching of the ETG with stellar mass $10^{11}\ {\rm M}_\odot$. However, this is not associated with a large increase in the large-scale gravitational stability, which is between $Q = 9$ and $Q = 15$ for all ETGs, both quenched and unquenched. To determine the source of the support against gravitational collapse in the quenched ETG, we can calculate and compare the contributions to the energy budget of the overdense star-forming gas ($\rho_{\rm gas} > 100\ {\rm cm}^{-3}$) made by the internal kinetic energy, self-gravity and external gravity due to the galactic potential, for each of our simulated galaxies. This approach is motivated by the general form of the virial theorem, as invoked by Meidt et al. (2018); Liu et al. (2021a), and given by

$$\frac{\ddot{I}}{2} = 2E_k + \int_V \left(\vec{a}(\vec{d}) \cdot \vec{d}\right) {\rm d}m, \tag{10}$$

where I is the moment of inertia of the cloud, E_k is its total kinetic energy, $\vec{d}$ is the position vector of a fluid element with respect to the centre of mass of the overdensity, and $\vec{a} = \ddot{\vec{d}}$ is the acceleration of that fluid element relative to the centre of mass. The volume integral is taken over the entire overdensity, such that $\int_V {\rm d}m = M$ for an overdensity of mass M. If the time-averaged $\ddot{I}(t)$ is equal to zero then an overdensity is in a state of equilibrium; if $\ddot{I} > 0$ then it is *expanding*, and if $\ddot{I} < 0$ then it is *collapsing*. Thus, we can write the condition for the collapse of star-forming overdensities as

$$\begin{aligned} 0 &> 2E_k + U_{\rm sg} + U_{R,{\rm ext}} + U_{z,{\rm ext}} \\ &= 2E_k + \int_V \vec{a}_{\rm sg}(\vec{d}) \cdot \vec{d}\, {\rm d}m + \int_V \vec{a}_{R,{\rm ext}}(\vec{d}) \cdot \vec{d}\, {\rm d}m \\ &\quad + \int_V \vec{a}_{z,{\rm ext}}(\vec{d}) \cdot \vec{d}\, {\rm d}m, \end{aligned} \tag{11}$$

where $\vec{a}_{\rm sg}$ are the acceleration vectors of the fluid elements due to self-gravity, $\vec{a}_{R,{\rm ext}}$ are due to the external gravitational forces within the gas disk mid-plane, and $\vec{a}_{z,{\rm ext}}$ are due to the external gravitational forces perpendicular to the gas disk mid-plane. All terms are averaged over time. We may further divide the in-plane contribution from the external gravitational potential into an axisymmetric (ax) and a non-axisymmetric (nax) component, such that

$$U_{R,{\rm ext}} = U_{R,{\rm ext,ax}} + U_{R,{\rm ext,nax}}. \tag{12}$$

The energy contributions that are accounted for by the Toomre dispersion relation for an axisymmetric disk of non-negligible scale-height (e.g. Romeo & Wiegert 2011; Romeo & Falstad 2013) are therefore $U_{\rm sg}$, $U_{R,{\rm ext,ax}}$ and $U_{z,{\rm ext}}$, but not $U_{R,{\rm ext,nax}}$ or $U_{P,{\rm ext}}$.

Within our simulation, we compute the kinetic energy within an overdensity as

$$2E_k = \sum_i w_i m_i \langle(\vec{v}_i - \langle\vec{v}_i\rangle)^2\rangle, \tag{13}$$

where w_i are the kernel weights for each gas cell i in the overdensity such that $\sum_i w_i = 1$, m_i are the gas cell masses, $\vec{v}_i$ are their velocity vectors, $c_{s,i}$ are their sound-speeds, and $\gamma = 5/3$ is the polytropic index for our simulations. The energy contribution due to self-gravity is then

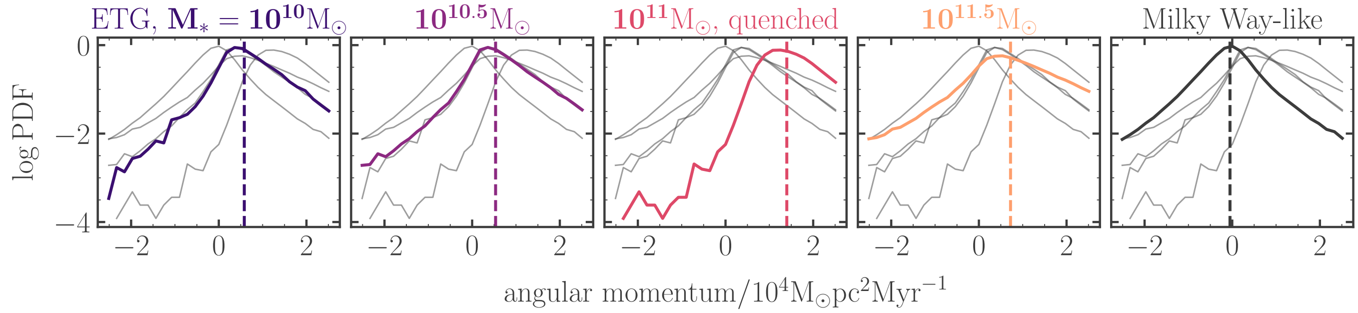

Figure 17. Probability density functions (PDFs) of the angular momentum of star-forming overdensities in five of our simulations, at a single snap-shot in time. The PDF for one simulation is highlighted in colour in each column. Dashed lines represent median values. Angular momenta > 0 are prograde (with galactic rotation), while angular momenta < 0 are retrograde (against galactic rotation). Only the values for overdensities with average star formation efficiencies SFE > 0.01 are shown.

$$U_{\rm sg} = \sum_i w_i m_i \sum_{j\neq i} -\frac{Gm_j}{|\vec{r}_{ij}|^3}(x_{ij}d_{x,i} + y_{ij}d_{y,i} + z_{ij}d_{z_i}), \tag{14}$$

where $\vec{r}_{ij} = (x_{ij}, y_{ij}, z_{ij})$ is the vector pointing from gas cell i to gas cell j, and $(d_{x,i}, d_{y,i}, d_{z,i})$ are the vector components of the position $\vec{d}_i$ of gas cell i with respect to the centre of mass of the overdensity. Similarly, the energy contribution due to external gravity perpendicular to the gas disk mid-plane is

$$U_{z,\rm ext} = \sum_i w_i m_i \Big(-\frac{\partial \Phi_{\rm ext}}{\partial z}\Big|_i d_{z,i}\Big), \tag{15}$$

where $\partial\Phi_{\rm ext}/\partial z|_i$ is the vertical gradient of the gravitational potential at the position of gas cell i, excluding the contribution due to the overdensity itself. The energy contributions due to the axisymmetric and non-axisymmetric components of the external gravitational potential within the disk mid-plane are then

$$\begin{aligned} U_{R,\rm ext,ax} = \sum_i w_i m_i \Big[&-\frac{\partial \Phi_{\rm ext}}{\partial x}\Big|_i d_{x,i} - \frac{\partial \Phi_{\rm ext}}{\partial y}\Big|_i d_{y,i} \\ &+ \Omega_0^2(x_i d_{x,i} + y_i d_{y,i})\Big] \end{aligned} \tag{16}$$

and

$$U_{R,\rm ext,nax} = \sum_i w_i m_i [-2\Omega_0(\dot{d}_{x,i} d_{y,i} - \dot{d}_{y,i} d_{x,i})], \tag{17}$$

where (x_i, y_i) is the in-plane position of gas cell i in the frame of the galaxy, and Ω_0 is the angular velocity of the centre of mass of the overdensity with respect to the galactic centre. Equation (16) quantifies the combined influence of the tidal and centrifugal forces, while Equation (17) quantifies the influence of the Coriolis force.

Using Equations (13)-(17), we compute the contribution of each energy term to the energy budget of all star-forming overdensities in all galaxies at one simulation time (400 Myr for the ETGs, 600 Myr for the Milky Way-like galaxy and 800 Myr for the NGC 300-like galaxy), to determine the time-averaged value of each. That is, we assume that the population of overdensities at each simulation time uniformly samples the time evolution of individual overdensities. The distributions of each energy term across each galaxy are shown in Figure 16.

Figure 16 demonstrates one reason that the Toomre Q parameters for our simulated galaxies are not good predictors of the level of morphological quenching: a large contribution to the energy budget of the overdensities comes from non-axisymmetric forces (Coriolis forces) due to the external gravitational in the galactic mid-plane, $U_{R,\rm ext,nax}$. These are not accounted for by the Toomre Q parameter, which is derived from an axisymmetric dispersion relation. In fact, these non-axisymmetric forces provide the largest contribution to the support of overdensities against collapse in the quenched galaxy (pink lines, centre column). As expected, the contribution of self-gravity is entirely compressive for all overdensities. The internal kinetic energy E_k and the combined tital and centrifugal forces ($U_{R,\rm ext}$) also provide support against this gravitational collapse. The vertical component of external gravity ($U_{z,\rm ext}$) is most commonly zero (corresponding to the galactic mid-plane) and may be positive or negative depending on position with respect to the mid-plane.

Figure 16 also demonstrates that the standard form of the virial parameter (Bertoldi & McKee 1992) is a poor predictor of the gravitational boundedness of overdensities or GMCs in ETGs. All of our simulated ETGs display comparable contributions against gravitational collapse from the external gravitational potential and from the internal kinetic energy; only the internal kinetic energy is considered as a source of support in the standard form of the virial theorem for GMCs. By contrast, the virial parameter is an excellent predictor of gravitational boundedness for overdensities in the Milky

Way-like galaxy, as the internal kinetic energy makes the only non-negligible contribution to support against gravitational collapse. This finding is in agreement with the analysis of Liu et al. (2021a) for observed GMCs in the lenticular galaxy NGC 4429, which demonstrated large differences between the standard virial parameter and an effective virial parameter that considers the influence of the external gravitational potential.

The role of the Coriolis force in providing support against gravitational collapse in the quenched ETG is also reflected in the higher prograde angular momentum of the star-forming overdensities in this simulation, shown in Figure 17. The median angular momentum of these overdensities in the quenched galaxy (centre) is three times that in the other ETGs. The median angular momentum of overdensities in the Milky Way-like simulation is zero, reflecting the negligible contribution made by the Coriolis force in that galaxy. These results are broadly in agreement with the results of (Liu et al. 2021b), who find that GMCs in the lenticular galaxy NGC 4429 have prograde angular momenta. By contrast, Utomo et al. (2015) find that GMCs are spun retrograde in NGC 4526.

6.3. *Cloud-scale criterion for morphological quenching*

In Figure 18 we show the star formation efficiencies in overdensities in our simulations as a function of their moments of inertia, computed via Equation (11). The black dashed line delineates net compressive (left) from net expansive (right) forces. We see that this line provides a much better predictor for the onset of morphological quenching than does the Toomre Q parameter: the galaxy that contains no gravitationally-bound gas is morphologically quenched, and cannot achieve star formation efficiencies above 10 per cent in its dense gas. We conclude that observations on the scales of GMCs are required to distinguish morphologically-quenched galaxies, as analysed in Utomo et al. (2015); Liu et al. (2021a) and Williams et al. (2023).

7. DISCUSSION AND SUMMARY

In this work we have presented six high-resolution chemo-dynamical simulations of galaxies spanning main sequence and quenched galactic environments. We have investigated their global properties: the regulation of star formation, the gas phase distribution and the gas phase morphology, related to the clustering of supernovae and the driving of galactic outflows. In this context, we have quantified the similarities and differences between the main sequence and quenched galaxies, with a view to modelling such environments in cosmological simulations. We can summarise our results as follows:

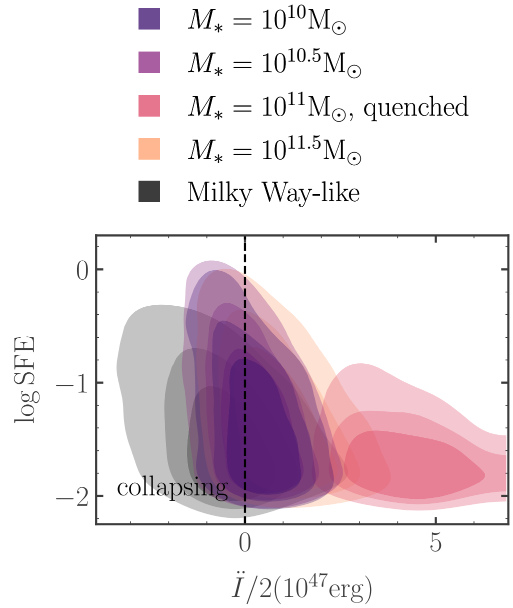

Figure 18. The 40%-60%-80% levels for the star formation efficiency (SFE) as a function of the moment of inertia $\ddot{I}/2$ for the overdensities with SFE > 0.01 in five of our simulations. The moment of inertia is calculated according to Equation (11), including supportive contributions from the external gravitational potential, as well as from internal kinetic energy. The dashed line at zero separates a net inward force on the overdensity ('collapsing') from a net outward force.

1. Aside from one morphologically-quenched ETG, the mid-plane pressure regulates star formation across both main sequence and early type environments, in agreement with Ostriker & Shetty (2011); Ostriker & Kim (2022). The relationship is much tighter than that between star formation and gas density.

2. The ETGs have galactic outflows with mass-loadings η that are reduced by up to four orders of magnitude, relative to main sequence galaxies. This is associated with an order of magnitude decrease in the strength of supernova clustering, which in turn is associated with an increase in disk gravitational stability Q.

3. The ETGs have a different equation of state to the main sequence galaxies, with a star-forming gas reservoir that is higher in density, lower in temperature, and richer in molecular gas.

4. Morphological quenching is driven by a combination of axisymmetric and non-axisymmetric forces at the scales of giant molecular clouds, preventing the gravitational collapse of the densest, molecu-

lar gas, and introducing prograde rotation of these overdensities.

Our conclusions have important implications for the modelling of star formation and stellar feedback across main sequence and quenched galactic environments in cosmological simulations:

1. The relationship between the mid-plane gas pressure and the star formation rate represents an improved model for star formation in cosmological simulations, relative to current models. The pressure-regulated model holds across both bulge-dominated and main sequence galactic environments, provided that the star formation efficiency is not morphologically-quenched.
2. The onset of morphological quenching introduces a transition away from the pressure-regulated regime, which depends non-linearly on the rotation curve Ω and on the level of gravitational stability Q.
3. Similarly, both the equation of state in the star-forming gas and the mass-loading of galactic outflows are mediated by the levels of supernova clustering, and so display non-linear variations with the mid-plane pressure and the level of gravitational stability Q.

I'm convinced that there must be a way to model the dependence of the equation of state on Ω (and possibly even the dependence of morphological quenching on Ω). If not analytically, then at least statistically, if we can probe the parameter space of Ω, $P_{\rm tot}$ and $n_{\rm H}$ more completely, with more high-resolution simulations. It would be good to talk with the AFM/ILI WGs about this...

ACKNOWLEDGEMENTS

We thank Volker Springel for providing us access to Arepo. SMRJ is supported by Harvard University through an Institute of Theory and Computation Fellowship. We thank Mark Krumholz and Romain Teyssier for helpful discussions. We thank Jiayi Sun for the use of his script for plotting beautiful density contours for Figures 11, 12 and 18.

REFERENCES

Bertoldi, F., & McKee, C. F. 1992, ApJ, 395, 140, doi: 10.1086/171638

Bigiel, F., Leroy, A., Walter, F., et al. 2008, AJ, 136, 2846, doi: 10.1088/0004-6256/136/6/2846

Bolatto, A. D., Wolfire, M., & Leroy, A. K. 2013, ARA&A, 51, 207, doi: 10.1146/annurev-astro-082812-140944

Cappellari, M., Emsellem, E., Krajnović, D., et al. 2011, MNRAS, 413, 813, doi: 10.1111/j.1365-2966.2010.18174.x

Cappellari, M., Scott, N., Alatalo, K., et al. 2013, MNRAS, 432, 1709, doi: 10.1093/mnras/stt562

Catinella, B., Saintonge, A., Janowiecki, S., et al. 2018, MNRAS, 476, 875, doi: 10.1093/mnras/sty089

Chabrier, G. 2003, PASP, 115, 763, doi: 10.1086/376392

Clark, P. C., Glover, S. C. O., & Klessen, R. S. 2012, MNRAS, 420, 745, doi: 10.1111/j.1365-2966.2011.20087.x

Colombo, D., Sanchez, S. F., Bolatto, A. D., et al. 2020, A&A, 644, A97, doi: 10.1051/0004-6361/202039005

Combes, F., Young, L. M., & Bureau, M. 2007, MNRAS, 377, 1795, doi: 10.1111/j.1365-2966.2007.11759.x

da Silva, R. L., Fumagalli, M., & Krumholz, M. 2012, ApJ, 745, 145, doi: 10.1088/0004-637X/745/2/145

da Silva, R. L., Fumagalli, M., & Krumholz, M. R. 2014, MNRAS, 444, 3275, doi: 10.1093/mnras/stu1688

Davé, R., Anglés-Alcázar, D., Narayanan, D., et al. 2019, MNRAS, 486, 2827, doi: 10.1093/mnras/stz937

Davé, R., Thompson, R., & Hopkins, P. F. 2016, MNRAS, 462, 3265, doi: 10.1093/mnras/stw1862

Davis, T. A., Greene, J. E., Ma, C.-P., et al. 2019, MNRAS, 486, 1404, doi: 10.1093/mnras/stz871

Davis, T. A., Alatalo, K., Bureau, M., et al. 2013, MNRAS, 429, 534, doi: 10.1093/mnras/sts353

Davis, T. A., Young, L. M., Crocker, A. F., et al. 2014a, MNRAS, 444, 3427, doi: 10.1093/mnras/stu570

—. 2014b, MNRAS, 444, 3427, doi: 10.1093/mnras/stu570

Davis, T. A., Gensior, J., Bureau, M., et al. 2022, MNRAS, 512, 1522, doi: 10.1093/mnras/stac600

Fielding, D., Quataert, E., & Martizzi, D. 2018, MNRAS, 481, 3325, doi: 10.1093/mnras/sty2466

Gensior, J., Kruijssen, J. M. D., & Keller, B. W. 2020, MNRAS, 495, 199, doi: 10.1093/mnras/staa1184

Gentry, E. S., Krumholz, M. R., Dekel, A., & Madau, P. 2017, MNRAS, 465, 2471, doi: 10.1093/mnras/stw2746

Glover, S. C. O., Federrath, C., Mac Low, M. M., & Klessen, R. S. 2010, MNRAS, 404, 2, doi: 10.1111/j.1365-2966.2009.15718.x

Glover, S. C. O., & Mac Low, M.-M. 2007a, ApJS, 169, 239, doi: 10.1086/512238

—. 2007b, ApJ, 659, 1317, doi: 10.1086/512227

Goldbaum, N. J., Krumholz, M. R., & Forbes, J. C. 2015, ApJ, 814, 131, doi: 10.1088/0004-637X/814/2/131

Gong, M., Ostriker, E. C., & Wolfire, M. G. 2017, ApJ, 843, 38, doi: 10.3847/1538-4357/aa7561

Grudić, M. Y., Hopkins, P. F., Faucher-Giguère, C.-A., et al. 2018, MNRAS, 475, 3511, doi: 10.1093/mnras/sty035

Hassan, S., Ostriker, E. C., Kim, C.-G., et al. 2023, MNRAS to be submitted

Hernquist, L. 1990, ApJ, 356, 359, doi: 10.1086/168845

Hopkins, P. F., Quataert, E., & Murray, N. 2011, MNRAS, 417, 950, doi: 10.1111/j.1365-2966.2011.19306.x

Jeffreson, S. M. R., & Kruijssen, J. M. D. 2018, MNRAS, 476, 3688, doi: 10.1093/mnras/sty594

Jeffreson, S. M. R., Krumholz, M. R., Fujimoto, Y., et al. 2021, MNRAS, 505, 3470, doi: 10.1093/mnras/stab1536

Jeffreson, S. M. R., Semenov, V. A., & Krumholz, M. R. 2023, arXiv e-prints, arXiv:2301.10251, doi: 10.48550/arXiv.2301.10251

Keller, B. W., & Kruijssen, J. M. D. 2020, arXiv e-prints, arXiv:2004.03608. https://arxiv.org/abs/2004.03608

Kennicutt, Jr., R. C. 1998, ApJ, 498, 541, doi: 10.1086/305588

Kim, C.-G., Kim, J.-G., Gong, M., & Ostriker, E. C. 2023a, ApJ, 946, 3, doi: 10.3847/1538-4357/acbd3a

Kim, C.-G., & Ostriker, E. C. 2015, ApJ, 815, 67, doi: 10.1088/0004-637X/815/1/67

Kim, C.-G., Ostriker, E. C., Somerville, R. S., et al. 2020, ApJ, 900, 61, doi: 10.3847/1538-4357/aba962

Kim, J.-G., Gong, M., Kim, C.-G., & Ostriker, E. C. 2023b, ApJS, 264, 10, doi: 10.3847/1538-4365/ac9b1d

Kim, J.-h., Abel, T., Agertz, O., et al. 2014, ApJS, 210, 14, doi: 10.1088/0067-0049/210/1/14

Koch, E. W., Rosolowsky, E. W., Lockman, F. J., et al. 2018, MNRAS, 479, 2505, doi: 10.1093/mnras/sty1674

Kruijssen, J. M. D., Schruba, A., Chevance, M., et al. 2019, Nature, 569, 519, doi: 10.1038/s41586-019-1194-3

Krumholz, M., & Burkert, A. 2010, ApJ, 724, 895, doi: 10.1088/0004-637X/724/2/895

Krumholz, M. R. 2013, DESPOTIC: Derive the Energetics and SPectra of Optically Thick Interstellar Clouds, Astrophysics Source Code Library. http://ascl.net/1304.007

—. 2014, MNRAS, 437, 1662, doi: 10.1093/mnras/stt2000

Krumholz, M. R., Burkhart, B., Forbes, J. C., & Crocker, R. M. 2018, MNRAS, 477, 2716, doi: 10.1093/mnras/sty852

Krumholz, M. R., Fumagalli, M., da Silva, R. L., Rendahl, T., & Parra, J. 2015, MNRAS, 452, 1447, doi: 10.1093/mnras/stv1374

Krumholz, M. R., & Matzner, C. D. 2009, ApJ, 703, 1352, doi: 10.1088/0004-637X/703/2/1352

Krumholz, M. R., & McKee, C. F. 2005, ApJ, 630, 250, doi: 2005ApJ...630..250K

Leroy, A. K., Schinnerer, E., Hughes, A., et al. 2021, ApJS, 257, 43, doi: 10.3847/1538-4365/ac17f3

Liu, L., Bureau, M., Blitz, L., et al. 2021a, MNRAS, 505, 4048, doi: 10.1093/mnras/stab1537

—. 2021b, MNRAS, 505, 4048, doi: 10.1093/mnras/stab1537

MacLaren, I., Richardson, K. M., & Wolfendale, A. W. 1988, ApJ, 333, 821, doi: 10.1086/166791

Martig, M., Bournaud, F., Teyssier, R., & Dekel, A. 2009, ApJ, 707, 250, doi: 10.1088/0004-637X/707/1/250

Martig, M., Crocker, A. F., Bournaud, F., et al. 2013, MNRAS, 432, 1914, doi: 10.1093/mnras/sts594

Matzner, C. D. 2002, ApJ, 566, 302, doi: 10.1086/338030

Meidt, S. E., Leroy, A. K., Rosolowsky, E., et al. 2018, ApJ, 854, 100, doi: 10.3847/1538-4357/aaa290

Monaghan, J. J. 1992, ARA&A, 30, 543, doi: 10.1146/annurev.aa.30.090192.002551

Murray, N., Quataert, E., & Thompson, T. A. 2010, ApJ, 709, 191, doi: 10.1088/0004-637X/709/1/191

Murray, N., & Rahman, M. 2010, ApJ, 709, 424, doi: 10.1088/0004-637X/709/1/424

Navarro, J. F., Frenk, C. S., & White, S. D. M. 1997, ApJ, 490, 493, doi: 10.1086/304888

Nelson, D., Pillepich, A., Springel, V., et al. 2018, MNRAS, 475, 624, doi: 10.1093/mnras/stx3040

Nelson, R. P., & Langer, W. D. 1997, ApJ, 482, 796, doi: 10.1086/304167

Ostriker, E. C., & Kim, C.-G. 2022, ApJ, 936, 137, doi: 10.3847/1538-4357/ac7de2

Ostriker, E. C., McKee, C. F., & Leroy, A. K. 2010, ApJ, 721, 975, doi: 10.1088/0004-637X/721/2/975

Ostriker, E. C., & Shetty, R. 2011, ApJ, 731, 41, doi: 10.1088/0004-637X/731/1/41

O'Sullivan, E., Combes, F., Salomé, P., et al. 2018, A&A, 618, A126, doi: 10.1051/0004-6361/201833580

Padoan, P., Federrath, C., Chabrier, G., et al. 2014, in Protostars and Planets VI, ed. H. Beuther, R. S. Klessen, C. P. Dullemond, & T. Henning, 77, doi: 10.2458/azu_uapress_9780816531240-ch004

Padoan, P., Haugbølle, T., Nordlund, Å., & Frimann, S. 2017, ApJ, 840, 48, doi: 10.3847/1538-4357/aa6afa

Phillips, T. G., Ellison, B. N., Keene, J. B., et al. 1987, ApJL, 322, L73, doi: 10.1086/185039

Piotrowska, J. M., Bluck, A. F. L., Maiolino, R., & Peng, Y. 2022, MNRAS, 512, 1052, doi: 10.1093/mnras/stab3673

Plummer, H. C. 1911, MNRAS, 71, 460, doi: 10.1093/mnras/71.5.460

Power, C., Navarro, J. F., Jenkins, A., et al. 2003, MNRAS, 338, 14, doi: 10.1046/j.1365-8711.2003.05925.x

Romeo, A. B., & Falstad, N. 2013, MNRAS, 433, 1389, doi: 10.1093/mnras/stt809

Romeo, A. B., & Wiegert, J. 2011, MNRAS, 416, 1191, doi: 10.1111/j.1365-2966.2011.19120.x

Russell, H. R., McNamara, B. R., Fabian, A. C., et al. 2016, MNRAS, 458, 3134, doi: 10.1093/mnras/stw409

—. 2019, MNRAS, 490, 3025, doi: 10.1093/mnras/stz2719

Safranek-Shrader, C., Krumholz, M. R., Kim, C.-G., et al. 2017, MNRAS, 465, 885, doi: 10.1093/mnras/stw2647

Saintonge, A., Tacconi, L. J., Fabello, S., et al. 2012, ApJ, 758, 73, doi: 10.1088/0004-637X/758/2/73

Saintonge, A., Catinella, B., Tacconi, L. J., et al. 2017, ApJS, 233, 22, doi: 10.3847/1538-4365/aa97e0

Salomé, P., & Combes, F. 2003, A&A, 412, 657, doi: 10.1051/0004-6361:20031438

Schaye, J., Crain, R. A., Bower, R. G., et al. 2015, MNRAS, 446, 521, doi: 10.1093/mnras/stu2058

Semenov, V. A., Kravtsov, A. V., & Diemer, B. 2022, ApJS, 261, 16, doi: 10.3847/1538-4365/ac69e1

Smith, M. C., Bryan, G. L., Somerville, R. S., et al. 2020, arXiv e-prints, arXiv:2009.11309. https://arxiv.org/abs/2009.11309

Smith, M. C., Fielding, D. B., Bryan, G. L., et al. 2023, arXiv e-prints, arXiv:2301.07116, doi: 10.48550/arXiv.2301.07116

Sobolev, V. V. 1960, Moving Envelopes of Stars, doi: 10.4159/harvard.9780674864658

Solomon, P. M., & Vanden Bout, P. A. 2005, ARA&A, 43, 677, doi: 10.1146/annurev.astro.43.051804.102221

Springel, V. 2010, MNRAS, 401, 791, doi: 10.1111/j.1365-2966.2009.15715.x

Springel, V., Di Matteo, T., & Hernquist, L. 2005, MNRAS, 361, 776, doi: 10.1111/j.1365-2966.2005.09238.x

Springel, V., & Hernquist, L. 2003, MNRAS, 339, 289, doi: 10.1046/j.1365-8711.2003.06206.x

Stone, J. M., & Gardiner, T. 2009, NewA, 14, 139, doi: 10.1016/j.newast.2008.06.003

Stone, J. M., Gardiner, T. A., Teuben, P., Hawley, J. F., & Simon, J. B. 2008, ApJS, 178, 137, doi: 10.1086/588755

Sun, J., Leroy, A. K., Ostriker, E. C., et al. 2020, arXiv e-prints, arXiv:2002.08964. https://arxiv.org/abs/2002.08964

—. 2023, ApJL, 945, L19, doi: 10.3847/2041-8213/acbd9c

Tacconi, L. J., Genzel, R., Saintonge, A., et al. 2018, ApJ, 853, 179, doi: 10.3847/1538-4357/aaa4b4

Thompson, T. A., Quataert, E., & Murray, N. 2005, ApJ, 630, 167, doi: 10.1086/431923

Utomo, D., Blitz, L., Davis, T., et al. 2015, ApJ, 803, 16, doi: 10.1088/0004-637X/803/1/16

Vogelsberger, M., Genel, S., Sijacki, D., et al. 2013, MNRAS, 436, 3031, doi: 10.1093/mnras/stt1789

Vogelsberger, M., Genel, S., Springel, V., et al. 2014, Nature, 509, 177, doi: 10.1038/nature13316

Welch, G. A., & Sage, L. J. 2003, ApJ, 584, 260, doi: 10.1086/345537

Westmeier, T., Braun, R., & Koribalski, B. S. 2011, MNRAS, 410, 2217, doi: 10.1111/j.1365-2966.2010.17596.x

Wiklind, T., & Rydbeck, G. 1986, A&A, 164, L22

Williams, T. G., Bureau, M., Davis, T. A., et al. 2023, arXiv e-prints, arXiv:2308.05146. https://arxiv.org/abs/2308.05146

Young, L. M., Bureau, M., Davis, T. A., et al. 2011, MNRAS, 414, 940, doi: 10.1111/j.1365-2966.2011.18561.x

APPENDIX

A. CHEMICAL POST-PROCESSING

As noted in Section 2.1, the CO-luminous gas fraction in our simulations is calculated in post-processing using the DESPOTIC model for astrochemistry and radiative transfer (Krumholz 2013). The self- and dust-shielding of CO molecules from the ambient UV radiation field cannot be accurately computed during run-time at the mass resolution of our simulation. Within DESPOTIC, the escape probability formalism is applied to compute the CO line emission from each gas cell according to its hydrogen atom number density $n_{\rm H}$, column density $N_{\rm H}$ and virial parameter $\alpha_{\rm vir}$, assuming that the cells are approximately spherical. In practice, the line luminosity varies smoothly with the variables $n_{\rm H}$, $N_{\rm H}$, and $\alpha_{\rm vir}$. We therefore interpolate over a grid of pre-calculated models at regularly-spaced logarithmic intervals in these variables to reduce computational cost. The hydrogen column density is estimated via the local approximation of Safranek-Shrader et al. (2017) as $N_{\rm H} = \lambda_{\rm J} n_{\rm H}$, where $\lambda_{\rm J} = (\pi c_s^2/G\rho)^{1/2}$ is the Jeans length, with an upper limit of $T = 40$ K on the gas cell temperature. The virial parameter is calculated from the turbulent velocity dispersion of each gas cell according to MacLaren et al. (1988); Bertoldi & McKee (1992). The line emission is self-consistently coupled to the chemical and thermal evolution of the gas, including carbon and oxygen chemistry (Gong et al. 2017), gas heating by cosmic rays and the grain photo-electric effect, line cooling due to C^+, C, O and CO and thermal exchange between dust and gas. We match the ISRF strength and cosmic ionisation rate to the values used in our live chemistry.

Having calculated values of the CO line luminosity for each simulated gas cell, we compute the CO-bright molecular hydrogen surface density as

$$\begin{aligned}\Sigma_{\rm H_2,CO}[{\rm M_\odot pc^{-2}}] =& \frac{2.3\times10^{-29}{\rm M_\odot}({\rm erg\ s^{-1}})^{-1}}{m_{\rm H}[{\rm M_\odot}]} \\ &\times \int_{-\infty}^{\infty} {\rm d}z' \rho_{\rm g}(z') L_{\rm CO}[{\rm erg\ s^{-1}\ H\ atom^{-1}}],\end{aligned} \tag{A1}$$

where $\rho_{\rm g}(z)$ is the total gas volume density in ${\rm M_\odot\ pc^{-3}}$ at a distance z (in pc) from the galactic mid-plane. The factor of 2.3×10^{-29} ${\rm M_\odot}$ $({\rm erg\ s^{-1}})^{-1}$ combines the mass-to-luminosity conversion factor $\alpha_{\rm CO} = 4.3\ {\rm M_\odot pc^{-2}(K\ kms^{-1})^{-1}}$ of Bolatto et al. (2013) with the line-luminosity conversion factor $5.31\times10^{-30}({\rm K\ kms^{-1}pc^2})/({\rm erg\ s^{-1}})$ for the CO $J = 1 \rightarrow 0$ transition at redshift $z = 0$ (Solomon & Vanden Bout 2005).

B. CALCULATION OF THE TOTAL MID-PLANE PRESSURE $P_{\rm TOT}$ AND THE INTERSTELLAR MEDIUM WEIGHT $\mathcal{W}$

In Figures 12 and 13 we show the total mid-plane pressure $P_{\rm tot}$ and the gravitational weight $\mathcal{W}$ of the interstellar medium across our simulation suite. These quantities are computed on a cylindrical three-dimensional grid in galactocentric radius R, azimuthal angle θ and vertical distance z from the galactic mid-plane. The R-bins have a width of 500 pc and a separation of 200pc, while the z-bins have a width of 10 pc and a separation of 10 pc. Eight θ bins with $\theta\in[0,2\pi]$ are used in every case.

The set of gas cells within each (R,θ,z) bin are used to compute the total volume-weighted mid-plane pressure as the sum of the thermal $P_{\rm th}$ and turbulent $P_{\rm turb}$ contributions, such that

$$P_{\rm tot} = P_{\rm th} + P_{\rm turb}, \tag{B2}$$

where

$$P_{\rm th} = \langle\rho\rangle_V \langle c_s^2\rangle_m, \tag{B3}$$

and

$$P_{\rm turb} = \langle\rho\rangle_V \langle(v_z - \langle v_z\rangle_m)^2\rangle_m, \tag{B4}$$

with ρ the gas volume density, c_s the gas sound-speed, v_z the gas velocity perpendicular to the galactic mid-plane, $\langle...\rangle_V$ denoting a volume-weighted average and $\langle...\rangle_m$ denoting a mass-weighted average. Gas that is gravitationally bound with $\alpha_{\rm vir} < 2$, or that is in the hot, feedback-heated phase with $T > 10^4$ K is excluded. We then compute the maximum value of $P_{\rm tot}$ along the z-axis in each bin of (R,θ).

Similarly, the interstellar medium weight is computed over the set of gas cells within each (R, θ, z) bin, such that

$$\mathcal{W} = \frac{1}{2}\Delta z \sum_{-z_{\rm max}}^{z_{\rm max}} \langle \rho \rangle_V(z) \frac{\partial \Phi}{\partial z}(z), \tag{B5}$$

where $z_{\rm max} = 300$ pc for the ETG simulations and 1.5 kpc for the Milky Way-like and NGC 300-like simulations, and

$$\frac{\partial \Phi}{\partial z}(z) = \sum_i \sum_{j \neq i} \Big(-\frac{G m_j}{|\vec{r}_{ij}|} \Big) \tag{B6}$$

, where $\vec{r}_{ij}$ are the position vectors pointing from each gas cell i in the bin to particle j, where $\sum_j$ is over all other gas, stellar and dark matter particles in the simulation, which have masses m_j. Gas that is gravitationally bound with $\alpha_{\rm vir} < 2$, or that is in the hot, feedback-heated phase with $T > 10^4$ K is excluded from the value of $\langle \rho \rangle_V$, but not from $\partial \Phi / \partial z$. The values presented in Figures 12 and 13 are medians over θ and simulation time.